JOURNAL OF GEOPHYSICAL RESEARCH, VOL. 104, NO. D8, PAGES 9169-9198, APRIL 27, 1999

# Prediction of the number of cloud droplets in the ECHAM GCM

Ulrike Lohmann,[1] Johann Feichter,[2] Catherine C. Chuang,[3] and Joyce E. Penner[4]

**Abstract.** In this paper a prognostic equation for the number of cloud droplets (CDNC) is introduced into the ECHAM general circulation model. The initial CDNC is based on the mechanistic model of *Chuang and Penner* [1995], providing a more realistical prediction of CDNC than the empirical method previously used. Cloud droplet nucleation is parameterized as a function of total aerosol number concentration, updraft velocity, and a shape parameter, which takes the aerosol composition and size distribution into account. The total number of aerosol particles is obtained as the sum of marine sulfate aerosols produced from dimethyl sulfide, hydrophylic organic and black carbon, submicron dust, and sea-salt aerosols. Anthropogenic sulfate aerosols only add mass to the preexisting aerosols but do not form new particles. The simulated annual mean liquid water path, column CDNC, and effective radius agree well with observations, as does the frequency distributions of column CDNC for clouds over oceans and the variations of cloud optical depth with effective radius.

## 1. Introduction

Hygroscopic aerosol particles, such as sulfate aerosols, can act as cloud condensation nuclei (CCN). The number of available CCN is one of the parameters that determine the droplet number concentration, albedo, precipitation formation, and lifetime of warm clouds. Anthropogenic emissions of sulfur dioxide have substantially increased the global mean burden of sulfate aerosols. The resulting sulfate aerosol forcing is of similar magnitude but of opposite sign to the forcing due to greenhouse gases [e.g., *Houghton et al.*, 1996]. This forcing results from scattering back solar radiation directly (direct aerosol forcing) and indirectly by modifying cloud properties. If cloud liquid water content remains constant, an increase in the number concentration of aerosol particles that act as CCN will lead to a larger concentration of cloud droplets with smaller radius. This will increase cloud reflectivity, thereby leading to a negative forcing (indirect cloud albedo effect). Additionally, if the droplets are smaller, the formation of precipitation is less efficient. Therefore the residence time of clouds with small droplets may be increased (indirect cloud lifetime effect).

Many studies have been focused on the indirect effect of anthropogenic sulfate aerosols [e.g., *Chuang et al.*, 1997; *Kogan and Kogan*, 1997; *Lohmann and Feichter*, 1997; *Rotstayn*, 1999]. The first studies of the indirect effect conducted with general circulation models (GCM) [e.g., *Boucher and Lohmann*, 1995] used an empirical relationship to relate the mass of sulfate aerosols to the number of cloud droplets. *Jones et al.* [1994] empirically relate the number of aerosol particles rather than the mass of sulfate aerosols to the number of cloud droplets. However, the number of aerosols is obtained from the mass of sulfate aerosols only, so their approach is comparable to *Boucher and Lohmann* [1995]. The global mean indirect cloud albedo effect in those first studies is found to be between -0.5 W $m^{-2}$ and -1.6 W $m^{-2}$.

In a next step, *Lohmann and Feichter* [1997] simulated the indirect sulfate aerosol effect by using a coupled cloud microphysics-sulfur cycle model. It was shown that this model is very sensitive to the parameterization of the autoconversion rate and cloud cover. The simulated change in liquid water path between experiments with natural sulfur emissions only and anthropogenic and natural sulfur emissions varied between 11% and 32%, depending on the parameterization of the autoconversion rate and the cloud cover. *Lohmann and Feichter* [1997] and *Rotstayn* [1999] separated the contributions of the indirect sulfate aerosol effect into the increase in cloud lifetime and change in cloud albedo. Both studies concluded that failure to account for the

[1]Atmospheric Science Program, Department of Physics, Dalhousie University, Halifax, Nova Scotia, Canada.

[2]Max Planck Institute for Meteorology, Hamburg, Germany.

[3]Lawrence Livermore National Laboratory, Livermore, California.

[4]Departments of Atmospheric, Oceanic and Space Sciences, University of Michigan, Ann Arbor.



Paper number 1999JD900046.
0148-0227/99/1999JD900046$09.00

effect in cloud lifetime may underestimate the indirect effect by 40-50%. The total indirect effect amounts to -2.1 W $m^{-2}$ in the work of *Rotstayn* [1999] and varies between -1.4 and -4.8 W $m^{-2}$, depending on the autoconversion rate and cloud cover parameterization used by *Lohmann and Feichter* [1997].

However, all those studies have in common that an increase in the sulfate aerosol mass inevitably increases the number of cloud droplets. Much of the sulfate aerosol mass is formed within drops, where it may simply add mass to preexisting aerosol particles but not increase aerosol number concentration. An empirical relationship between sulfate mass and droplet number concentrations does not account for all the complexity as the activation of sulfate aerosols depends on the presence of other soluble aerosol species such as sea-salt or organics, on the updraft velocity, and on the aerosol size spectrum. Moreover, sinks of cloud droplets, precipitation formation, or evaporation alter the relationship between sulfate aerosols and droplet number. Thus an increase in sulfur dioxide emissions might not result in an increase in the number of cloud droplets. Moreover, in the empirical approaches used so far, the sulfate aerosol mass is a surrogate for the total mass of aerosols present, assuming that sulfate is the dominant CCN, and the ratio of sulfate mass to the total mass of aerosols is constant. There is observational evidence for a non-linear relationship between sulfate aerosol mass and total aerosol mass [e.g., *Li et al.*, 1996]. However, the fraction of the total aerosol mass comprised by sulfate is quite variable, ranging from 14% to 100% [*Hegg et al.*, 1993; *Malm et al.*, 1994; *Hegg et al.*, 1995; *Warneck*, 1988]. Even though *Hegg et al.* [1995] find that sulfate makes up, on average, 62% of the total mass of accumulation mode particles, they conclude that in their limited data set, most of the CCN were not sulfate.

Therefore a mechanistic relationship between sulfate mass increase and cloud droplet number increase is needed. The interactions between aerosols and cloud droplets must be based on physical principles rather than empirical relationships. One way to obtain a more realistic estimate of the number of cloud droplets is to predict it prognostically in a GCM. Such an approach was used by *Ghan et al.* [1997]. However, they assumed a constant aerosol number concentration of 300 $cm^{-3}$.

In this paper the formation of cloud droplets is linked to the calculated three-dimensional aerosol distribution by introducing a prognostic equation for the number of cloud droplets into the ECHAM general circulation model. This prognostic treatment allows for cloud droplet nucleation, advection of cloud droplets, droplet evaporation and collision-coalescence of cloud droplets. Thus the number of cloud droplets is estimated more realistically than if it is related empirically to the mass of sulfate aerosols. We use the total number of aerosol particles as given by the sum of maritime sulfate aerosols, soluble carbonaceous aerosols, submicron sea-salt, and submicron dust aerosols to estimate droplet nucleation according to *Chuang and Penner* [1995].

In the parameterization of droplet nucleation, information about aerosol size and composition is considered in a factor $\alpha$. Previous studies using this parameterization either obtained this factor from observations [*Lin and Leaitch*, 1997], assumed it to be constant [*Lohmann et al.*, 1999], or used a simple function of temperature alone [*Wyser*, 1998]. *Wyser* [1998] concluded that an $\alpha$ factor, depending on temperature, can explain cloud-to-cloud variability. In this study it is obtained from a microphysical model to allow for an internally mixed aerosol when anthropogenic sulfate condenses onto a preexisting particle.

The ECHAM4 general circulation model, the different aerosol species, the cloud scheme used in this study, and the treatment of aerosol and cloud optical properties are explained in section 2. A model validation of this integration in terms of aerosol optical thickness, the effective radius of cloud droplets, liquid water path, shortwave cloud forcing, and the variation of the effective radius with optical depth is given in section 3. Sensitivity studies, which vary all the variables used in the droplet nucleation parameterization, the number of aerosol particles, the updraft velocity, and the assumption of different size spectra for maritime and continental aerosols, are described in section 4. Discussion and conclusions are given in section 5.

## 2. Model Descriptions

### 2.1. Meteorological Model

The dynamics and part of the model physics of the ECHAM model have been adopted from the European Centre for Medium-Range Weather Forecasts (ECMWF) model [*Roeckner et al.*, 1996]. Prognostic variables are vorticity, divergence, temperature, (logarithm of) surface pressure, and the mass mixing ratios of water vapor, cloud liquid water, and cloud ice. The model equations are solved on 19 vertical levels in a hybrid $p$-$\sigma$-system by using the spectral transform method with triangular truncation at wavenumber 30 (T30). Nonlinear terms and physical processes are evaluated at grid points of a "Gaussian grid" providing a nominal resolution of 3.75° × 3.75°. A semi-implicit leap frog time integration scheme with $\Delta t$=30 min is used for the simulation with T30 resolution. Cumulus clouds are represented by a bulk model, including the effects of entrainment and detrainment on the updraft and downdraft convective mass fluxes [*Tiedtke*, 1989]. An adjustment closure based on the convective available potential energy (CAPE) is used [*Nordeng*, 1994]. Organized entrainment is assumed to depend on buoyancy, and the parameterization of organized detrainment is based on a cloud population hypothesis. The turbulent transfer of momentum, heat, water vapor, and total cloud water is calculated on the basis of a higher-order closure scheme [*Brinkop and Roeckner*, 1995]. The radiation code is based on a two-stream solution of the radiative transfer equation with six spectral intervals in the ter-

restrial infrared spectrum [*Morcrette,* 1991] and two in the solar part of the spectrum [*Fouquart and Bonnel,* 1980]. Gaseous absorption due to water vapor, $CO_2$, $O_3$, $CH_4$, $N_2O$, and CFCs is included, as well as scattering and absorption due to prescribed aerosols and model-generated clouds. The cloud optical properties are described below. ECHAM4 uses a semi-Lagrangian technique [*Rasch and Williamson,* 1990] for computing the horizontal and vertical advection of positive definite quantities such as water vapor, cloud liquid water, the number of cloud droplets, cloud ice, and all trace gases and aerosols included in this study.

### 2.2. Aerosol Physics

Dust and sea-salt are prescribed as three-dimensional monthly mean data, while prognostic equations are used to calculate the mass of sulfate and carbonaceous aerosols. The number concentration of the combined aerosol, which is needed for droplet nucleation, is obtained according to *Chuang et al.* [1997]. The individual aerosol species are described in the following subsections.

**2.2.1. Sulfur chemistry.** The parameterization of the sulfur chemistry is described in detail by *Feichter et al.* [1996]. Transport, dry and wet deposition, and chemical transformations of the constituents are calculated on-line with the GCM. Prognostic variables are dimethyl sulfide (DMS) and sulfur dioxide ($SO_2$) as gases and sulfate as an aerosol. The transport of these species due to advection, vertical diffusion, and convection is treated in the same way as the transport of water vapor. Biogenic emissions from the oceans and from soils and plants are assumed to occur as DMS. Seawater concentrations are prescribed according to *Kettle et al.* [1996], and the gas exchange is calculated according to [*Liss and Merlivat,* 1996]. Emissions from volcanoes, from biomass burning and from combustion of fossil fuel and from smelting occur as $SO_2$ [*Feichter et al.*, 1996; 1997]. As shown in Table 1, present-day emissions amount globally to 96 Tg S $yr^{-1}$, 70% of which are due to anthropogenic activities. The anthropogenic emissions are representative for the year 1985.

The dry deposition flux to the ground is assumed to be proportional to both the concentration in the lowest model layer (30 m above ground) and to a prescribed dry deposition velocity. For sulfate aerosol this is assumed to be 0.025 cm $s^{-1}$ over dry surfaces and 0.2 cm $s^{-1}$ over wetted surfaces and melting snow or ice, and for $SO_2$, it is 0.1 cm $s^{-1}$ and 0.8 cm $s^{-1}$, respectively [*Ganzeveld et al.,* 1998].

Removal of $SO_2$ and sulfate by precipitation is calculated explicitly in terms of the model's precipitation formation rate [*Feichter et al.,* 1996]. DMS as well as $SO_2$ in the gaseous phase are oxidized by reaction with hydroxyl (OH) during the day. Additionally, DMS reacts with nitrate radicals ($NO_3$) at night. It is assumed that the only end product of DMS oxidation is $SO_2$, while in reality, DMS can also be oxidized to MSA (as well as other oxidation products for which the yield is small and very uncertain). The consequence of this assumption is that $SO_2$ and sulfate may be slightly overestimated in marine regions. Two studies of the global sulfur cycle consider the oxidation pathway to MSA and found that only about 5% of the DMS is transformed to MSA [*Chin et al.,* 1996; *Pham et al.,* 1995].

Dissolution of $SO_2$ within cloud water is calculated according to Henry's law. In the aqueous phase, oxidation of $SO_2$ by hydrogen peroxide ($H_2O_2$) and ozone ($O_3$) is considered. Three-dimensional monthly mean oxidant concentrations are prescribed on the basis of calculations with ECHAM and a more comprehensive chemical model [*Roelofs and Lelieveld,* 1995]. The calculation of the reaction rates and the effective Henry's law constant for $SO_2$ requires assumptions about the cloud pH. Assuming that aqueous phase equilibria and electroneutrality are maintained and introducing the simplification that $[S(IV)] = [HSO_3^-]$, which can be applied if the pH ranges between 3 and 5, $[H^+]$ is approximated by assuming a molar ratio between sulfate and ammonium of 1 [*Dentener and Crutzen,* 1994]. The end product of the gaseous and aqueous oxidation of $SO_2$ is sulfate (for a more detailed description, see *Feichter et al.* [1996]). As sulfate is mainly present in the form of ammonium sulfate, the calculated sulfate mass mixing ratio is multiplied by the ratio of the molar weight of $(NH_4)_2SO_4/SO_4$ to convert the sulfate mass mixing ratio into an ammonium sulfate mass mixing ratio.

**2.2.2. Carbonaceous aerosols.** The aerosol module used to simulate the carbonaceous aerosol is described by *Cooke and Wilson* [1996]. In this study, prognostic equations are solved for hydrophylic (=soluble) and hydrophobic (=insoluble) organic and black

**Table 1.** Global Emissions of Sulfur Gases

| Species | Source | Reference | Tg S $yr^{-1}$ |
|---|---|---|---|
| Natural | | | |
| DMS | marine biosphere | *Kettle et al.* [1996] | 17.3 |
| DMS | terrestrial biosphere | *Spiro et al.* [1992] | 0.9 |
| $SO_2$ | noneruptive volcanoes | *Spiro et al.* [1992], *Graf et al.* [1997] | 8.0 |
| Anthropogenic | | | |
| $SO_2$ | biomass burning | *Hao et al.* [1990] | 2.5 |
| $SO_2$ | fossil fuel use and smelting | *Benkovitz et al.* [1994] | 66.8 |
| Total | | | 95.5 |

**Table 2.** Global Emissions of Carbonaceous Aerosols

| Species | Source | Reference | Tg C $yr^{-1}$ |
|---|---|---|---|
| BC | anthropogenic | *Liousse et al.* [1996] | 6.1 |
| BC | biomass burning | *Liousse et al.* [1996] | 5.6 |
| Total BC | | | 11.7 |
| OC | anthropogenic | *Liousse et al.* [1996] | 29.6 |
| OC | biomass burning | *Liousse et al.* [1996] | 59.3 |
| OC | natural | *Guenther et al.* [1995] | 16.2 |
| Total OC | | | 105.1 |

carbon, respectively. The carbonaceous aerosol module allows for emission of both hydrophobic and hydrophilic aerosol. Indeed, fossil fuel particulate carbon may be predominantly hydrophobic, but a certain fraction of the emissions are probably hydrophilic [*Cachier et al.*, 1996]. Black and organic carbon have various compounds attached to the surface [*Smith et al.*, 1989] which may determine their atmospheric behavior and also allow a chemical change in the properties of the surface layer as it ages in the atmosphere. Emissions of black carbon (BC) are assumed to be 80% hydrophobic and 20% hydrophylic. It is assumed that 50% of the organic carbon (OC) emissions are hydrophobic and 50% hydrophilic. Emissions have been calculated for 185 countries for the domestic, industrial, and transport sectors using a fuel usage database published by the United Nations. Some inconsistencies were found for a small number of countries with regard to the distribution of fuel usage between the industrial and the domestic sectors. Care has been taken to correct for this, using data from the fuel use database for the period 1970-1990. Emissions based on total particulate matter and submicron emission factors have been calculated. Global annual mean primary black carbon emissions from fossil fuel combustion amount to 6.1 Tg C $yr^{-1}$ [*Penner et al.*, 1993] and associated organic carbon emissions to 29.6 Tg C $yr^{-1}$ using submicron emission factors (Table 2) [*Liousse et al.*, 1996]. The emissions are representative of the year 1980. No seasonality in fossil fuel emissions are assumed at this point. One should keep in mind that primary organic aerosols represent only a fraction of the organic aerosols. Secondary production may account for up to 50% of the organic aerosol close to the anthropogenic source regions and even more at remote sites [*Liousse et al.*, 1996]. Additional carbon emissions due to biomass burning are assumed to be 5.6 Tg C $yr^{-1}$ for BC and 59.3 Tg C $yr^{-1}$ for OC, as given by *Liousse et al.* [1996]. As for the fossil fuel particulate emissions, we assume that 80% of BC and 50% of OC from biomass burning are emitted as hydrophobic. Natural OC from monoterpene emissions [*Guenther et al.*, 1995] account for 16.2 Tg C $yr^{-1}$.

A certain fraction of the freshly emitted carbonaceous aerosol is hydrophobic. These aerosols become hydrophylic after soluble compounds have been attached to the aerosol surface. The typical exponential aging time, until a hydrophobic aerosol becomes hydrophylic, has been assumed as 40 hours [*Cooke and Wilson*, 1996]. The aerosol lifetime is assumed to be governed by wet and dry deposition and no chemical sinks are used in this work. Precipitation scavenging of hydrophilic carbon is calculated explicitly in terms of the model's local precipitation formation rate, as is done for sulfates. The dry deposition flux to the ground is assumed to be proportional to both the concentration in the lowest model layer (30 m above ground) and the prescribed dry deposition velocity. For hydrophilic carbonaceous aerosol this is assumed to be 0.025 cm $s^{-1}$ over dry surfaces and 0.2 cm $s^{-1}$ over wetted surfaces and melting snow or ice (L. Ganzeveld, personal communication, 1998). Hydrophobic aerosols are deposited by a constant velocity of 0.025 cm $s^{-1}$ as the hydrophobic aerosols are assumed not to be influenced by wetted surfaces.

**2.2.3. Dust aerosols.** Dust is prescribed as monthly mean three-dimensional distributions. This distribution was calculated from an inventory for desert regions of the world. First, dust source regions were identified from the 1° x 1° soil moisture data of *Webb et al.* [1993] as those regions that perennially contain < 15 mm soil moisture. This soil moisture cutoff is somewhat arbitrary but gives regional outlines of dust sources that largely agree with those that have been identified and used by previous researchers [e.g., *Pye et al.*, 1987; *Joussame*, 1990; *Goudie and Wells*, 1995; *Tegen and Fung*, 1994]. We focused only on perennially dry areas to avoid the difficulty of modeling dust flux from regions where soil moisture and vegetation vary seasonally and hence greatly complicate dust flux estimation [e.g., *Gillette and Passi*, 1988; *Westphal et al.*, 1988]. Despite this limitation, it is thought that the arid areas identified by the above method contribute the vast majority of dust flux to the atmosphere [e.g., *Pye*, 1987].

Mobilization of dust has been calculated on the basis of monthly mean surface wind speeds (at 10 m height) within the above-identified source regions from a 10 year history 1979-1988 generated using the European Center for Medium-Range Weather Forecasting model at T42

resolution (approximately 2.8° x 2.8°) [*Phillips*, 1994]. Based largely on the theoretical and empirical work of *Westphal et al.* [1988], an algorithm was developed relating these mean wind speeds to mean monthly dust source strength (g $cm^{-2}$ $s^{-1}$):

$$F_x = D\,C\,W\,E\,G\,(k\,V)^4 \quad (1)$$

where $F_x$ is the flux of dust particles with radii in the range $x$, $D$ is the fraction of dust which can be mobilized (=0.13) [*Westphal et al.*, 1988], C is the fraction of total dust source relevant to size class (=0.01 for 0.1-1 $\mu$m particles; =0.2 for 1-10 $\mu$m particles) [*Schütz*, 1979; *Jaenicke*, 1988], $W$ is the fraction of model grid with soil water always < 15 mm [*Webb et al.*, 1993], $E$ is an empirical correction factor; initially equal to 22.3 x $10^{-14}$ [*Westphal et al.*, 1988] but adjusted in some areas to account for long-term weathering and land use changes, $G$ is the wind gustiness correction equal to $(0.499 + 0.013 \exp(21.1/V))^{-1}$ [*Gillette*, 1992], $k$=6.38 [*Westphal et al.*, 1988], and $V$ is the mean monthly surface friction velocity, m $s^{-1}$.

The mean monthly wind speeds at 10 m were converted to ground surface friction velocities $V$ using the logarithmic relationship described by *Westphal et al.* [1988]. A threshold friction velocity below which dust is not mobilized was assumed to be 50 cm $s^{-1}$. This value is a rough average of widely varying values for arid soils [e.g., *Gillette and Passi*, 1988; *Nickling and Gilles*, 1989]. The gustiness factor $G$ is a very nonlinear function of mean surface wind speed ranging from 0 to 2 and was used to multiply the dust flux generated from mean monthly wind speeds. This takes into account stochastic variation in wind speed (and associated, nonsymmetrical dust flux) about the monthly mean [*Gillette*, 1992]. Dust flux was assumed to be proportional to the fourth power of the mean surface friction velocity [*Westphal et al.*, 1988]. Finally, total dust flux, $F_t = F_{0.1-1\mu m} + F_{1-10\mu m}$.

Observations indicate that injection of dust can occur over deep atmospheric layers. Therefore we assumed a uniform vertical injection rate of the 0.1-1 $\mu$m particles between the surface and 600 hPa, and a linearly decreasing injection rate to zero at 600 hPa for the 1-10 $\mu$m particles is assumed. The linearly decreasing injection rate is a simplified method to account for the fact that larger particles are not lifted as easily as those in the small particle range. Predicted particle dry deposition velocities range from $10^{-3}$ cm $s^{-1}$ to 10 cm $s^{-1}$ [*Sehmel*, 1984], depending on particle size and atmospheric conditions. A prescribed deposition velocity of 0.1 cm $s^{-1}$ is used for particles in the size range 0.1-1 $\mu$m, and deposition velocity for particles in the range $1 < r < 10$ $\mu$m was set to 1 cm $s^{-1}$, roughly in midrange of the velocities predicted for these particle sizes [*Sehmel*, 1984; *Slinn and Slinn*, 1980]. In addition, the particles experienced a settling velocity, calculated using formulas available in the work of *Pruppacher and Klett* [1978].

In addition to dry deposition, dust particles can be scavenged by precipitation. Large-scale and convective precipitation scavenging coefficients that are consistent with less efficient scavenging for dust relative to other aerosols (e.g., sulfate aerosols), namely 2.5 and 0.7 $cm^{-1}$, respectively, for the 0.1-1 $\mu$m particles [*Penner et al.*, 1993] are used. Larger particles, however, should be more easily scavenged [*Pruppacher and Klett*, 1978]. The scavenging coefficients for the 1-10 $\mu$m particle particles are equal to 7.5 and 2.1 $cm^{-1}$ for large-scale and convective scavenging, respectively.

Initial results from the model showed significant deviations from observations in three regions. Modeled dust concentration, dust deposition, and optical depth downwind from Asia was found to be lower than observations by roughly a factor of 5. One explanation for this is that the efficiency of dust generation from the Asian continent is greater than in the Sahara (the primary source for the model parameter values used here (equation 1)) due to tectonic activity, periglacial processes, and human impacts [*Pye*, 1987; *Tegen and Fung*, 1994]. Thus we felt justified in increasing the empirical correction factor $E$ in equation (1) to 112 x $10^{-14}$ in this region.

In contrast, it was evident that dust generation from Australia was too high by about a factor of 10. The paucity of dust from this region relative to other arid dust source areas has been previously noted [e.g., *Pye et al.*, 1987; *Prospero et al.*, 1989; *Tegen and Fung*, 1994; *Rea*, 1994] and may reflect the relative tectonic stability, low weathering rates, duration of land surface exposure, and low human impacts in this area. For this reason we lowered the value $E$ for Australia to 2.2 x $10^{-14}$. Finally, it was evident that the modeled South African source was also too strong, again by roughly a factor of 10, and the $E$ used for this region was reduced accordingly.

In this study, only dust aerosols below 1 $\mu$m in radius are considered. In order to apply the parameterization of *Chuang and Penner* [1995] in a consistent manner, the dust mass was reduced to 42%, before it was converted into an aerosol number concentration.

**2.2.4. Sea-Salt aerosols.** Sea-salt aerosols are prescribed as three-dimensional monthly mean fields, which are obtained from simulations with GRANTOUR. The main mechanism for sea-salt generation, for aerosol size $r < 10$ $\mu$m, is via the bursting of whitecap bubbles. *Monahan et al.* [1986] used measurements of the production of droplets in a whitecap simulation tank to estimate

$$\frac{dF}{dr} = 1.373\,V^{3.41} r^{-3} (1 + 0.057 r^{1.05}) 10^{1.19 \exp(-B^2)} \quad (2)$$

where

$$B = (0.38 - \log r)/0.650 \quad (3)$$

In these equations, $\frac{dF}{dr}$ is the mass flux of sea-salt per unit increment in radius (g $m^{-2}$ $\mu m^{-1}$ $s^{-1}$), $V$ is the 10 m wind speed (m $s^{-1}$), and $r$ is the aerosol radius ($\mu$m).

This estimate of sea-salt generation was combined with the 10 year monthly averaged surface wind speed from the ECMWF model [*Phillips*, 1994] and an estimate of wind speed variation from the monthly average [*Pavia and O'Brien*, 1986]:

$$f(V,\overline{V},C) = \frac{C}{\overline{V}}\left(\frac{\overline{V}}{C}\right)^{(C-1)} \exp\left(-\left[\frac{V^C}{\overline{V}}\right]\right) \quad (4)$$

In this expression, $C$=2, and $\overline{V}$ is the monthly mean wind speed at 10 m. Thus

$$\frac{d\overline{F}}{dr}(\overline{V},r) = \int_0^\infty f(V,\overline{V},C)\frac{dF}{dr}(V,r)dV \quad (5)$$

These formulas were used to generate sea-salt in two model bins: 0-1 $\mu$m and 1-10 $\mu$m radius. In this study, only sea-salt in the first model bin is considered. Settling and deposition were similar to those used for dust, while the precipitation scavenging coefficients were set to 2.5 and 0.7 $cm^{-1}$, respectively, for the 0.1-1 $\mu$m particles. The scavenging coefficients for the 1-10 $\mu$m particles are 3 times those of the smaller particle size, or 7.5 and 2.1 $cm^{-1}$ for large-scale and convective scavenging, respectively.

### 2.3. Cloud Scheme

The cloud scheme used in this study is a modified version based on that discussed by *Lohmann and Roeckner* [1996]. Prognostic variables are cloud liquid water $q_l$, cloud ice $q_i$, and the number of cloud droplets $N_l$. Parameterized microphysical processes are condensational growth of cloud droplets, depositional growth of ice crystals, homogeneous and heterogeneous freezing of cloud droplets, autoconversion of cloud droplets, aggregation of ice crystals, accretion of cloud ice and cloud droplets by snow, of cloud droplets by rain, evaporation of cloud liquid water and rain, sublimation of cloud ice and snow, and melting of cloud ice and snow. The precipitation formation rates for mixed and ice clouds are adopted from the formulation used in the mesoscale model GESIMA (Geesthacht simulation model of the atmosphere) [*Levkov et al.*, 1992].

In the work of *Lohmann and Feichter* [1997] the number of cloud droplets ($N_l$) was empirically related to the sulfate aerosol mass ($SO_4^{2-}$) [*Boucher and Lohmann*, 1995] as obtained from measurements of $SO_4^{2-}$, CCN, and $N_l$ taken at various continental and marine sites in clean and polluted air for a variety of weather situations. To describe the relationship between aerosol number concentration and cloud droplet nucleation more realistically, the following prognostic equation for the number of cloud droplets with the respective sources and sinks is introduced:

$$\frac{\partial N_l}{\partial t} = R(N_l)+Q_{\rm nucl}-Q_{\rm autn}-Q_{\rm self}-\frac{N_l}{q_l}(Q_{\rm racl}+Q_{\rm sacl}+Q_{\rm frz}+Q_{\rm evc})+Q_{\rm mlt} \quad (6)$$

$R(N_l)$ represents the advective, turbulent, and convective transports of $N_l$. Convective transport refers to the detrainment at the top of cumulus clouds. A mean cloud droplet volume radius of 10 $\mu$m is assumed to obtain the cloud droplet number concentration in accordance with the detrained liquid water content. The microphysical processes are nucleation of cloud droplets $Q_{\rm nucl}$, autoconversion of cloud droplets $Q_{\rm autn}$, self-collection of cloud droplets $Q_{\rm self}$, accretion of cloud droplets by rain $Q_{\rm racl}$ and snow $Q_{\rm sacl}$, respectively, freezing of cloud droplets $Q_{\rm frz}$ and melting of ice crystals $Q_{\rm mlt}$, and evaporation of cloud droplets $Q_{\rm evc}$. The conversion rates in terms of the liquid water mixing ratio are described by *Lohmann and Roeckner* [1996]. It is assumed that the cloud droplet number concentration is depleted proportional to the liquid water mixing ratio. In case of evaporation, this should mimic heterogeneous evaporation where some droplets from all size categories evaporate [*Hudson and Rogers*, 1986]. For melting of ice crystals also a mean cloud droplet volume radius of 10 $\mu$m is chosen to obtain the cloud droplet number concentration in accordance with the melted cloud ice.

The parameterization of the autoconversion of cloud droplets used for the depletion in liquid water mixing ratio ($Q_{\rm autw}$) in the work of *Lohmann and Roeckner* [1996] is derived from the stochastic collection equation, which describes the time evolution of a droplet spectrum changing by collisions among droplets of different size [*Beheng*, 1994].

Following the treatment of *Beheng* [1994] the change in cloud droplet number concentration ($Q_{\rm autn}$) and self-collection of cloud droplets ($Q_{\rm self}$) are parameterized as (in SI units)

$$Q_{\rm autn} = 7.7\times10^9\,\rho\,Q_{\rm autw} \quad (7)$$

$$Q_{\rm self} = 1.29\times10^{10}\,(\rho\,\frac{q_l}{b})^2 \quad (8)$$

where $\rho$ is the air density, and $b$ is the fractional cloud cover.

The nucleation rate of cloud droplets $Q_{\rm nucl}$ is based on the total number of aerosols $N_a$ ($cm^{-3}$), the updraft velocity $w$ (cm $s^{-1}$) and a factor $\alpha$, which takes the aerosol composition and size spectrum into account [*Chuang and Penner*, 1995]:

$$Q_{\rm nucl} = \max\left(\frac{1}{\Delta t}\frac{N_a w}{w+\alpha N_a} - N_{\rm old}, 0\right) \quad (9)$$

Nucleation is only calculated at cloud base when condensation occurs. The amount of droplets nucleated is assumed to be constant throughout the depth of the cloud to mimic the internal circulation inside the

cloud. In old clouds, only new droplets are formed if the number that would be activated at cloud base exceeds the number of preexisting cloud droplets at cloud base ($N_{old}$).

The vertical velocity is given as the sum of the grid mean vertical velocity and a sub-grid-scale vertical velocity. We assume that the sub-grid-scale vertical velocity is dominated by the turbulent transports and choose the root-mean-square value of the turbulent kinetic energy (TKE) as a measure of this, so $w = \overline{w} + c\sqrt{TKE}$ with $c$=0.7 [*Lohmann et al.*, 1999]. However, in the layer closest to the surface, $w$ is calculated from the grid mean vertical velocity only to avoid spurious cloud development near the surface. Using only one updraft velocity for the whole grid cell instead of applying a probability distribution, as used by *Ghan et al.* [1997] and *Chuang et al.* [1997], is a simplification as the vertical velocity varies widely over a grid cell. The impact of vertical velocity will be investigated further in the sensitivity studies.

$N_a$ is obtained as the sum of marine sulfate aerosols produced from dimethyl sulfide, hydrophylic organic and black carbon, submicron dust, and submicron sea-salt aerosols as described in the previous section:

$$N_a^{\rm cnt} = \frac{m_{\rm OC}/\rho_{\rm OC} + m_{\rm BC}/\rho_{\rm BC} + m_{\rm DUST}/\rho_{\rm DUST}}{4/3\pi r_{\rm cnt}^3}$$
$$N_a^{\rm mar} = \frac{m_{\rm SS}/\rho_{\rm SS} + m_{\rm SULF}/\rho_{\rm SULF}}{4/3\pi r_{\rm mar}^3} \quad (10)$$

where the density of carbonaceous aerosols ($\rho_{\rm OC}$=$\rho_{\rm BC}$) is 1000 kg m$^{-3}$, of sulfate aerosols ($\rho_{\rm SULF}$) is 1769 kg m$^{-3}$, of sea-salt ($\rho_{\rm SS}$) and dust ($\rho_{\rm DUST}$) is 2000 kg m$^{-3}$. The volume mean radius for submicron particles adapted in this study is 0.085 $\mu$m for the maritime aerosol and 0.052 $\mu$m for the continental aerosol. The difference in hygroscopicity between individual aerosol components is accounted for in the different parameterization of alpha for the continental and marine aerosols; that is, the number of activated cloud droplets levels off faster with increasing $N_a$ over land than over oceans, because of the mainly insoluble dust.

Beyond that, we assume that a minimum number of 300 aerosol particles per cm$^{-3}$ is always available, which is the concentration of the background aerosol number concentration given by *Jaenicke* [1993]. Sulfate particles produced from continental sources of sulfur dioxide are not included in $N_a$ because the amount of preexisting particles in those regions is so high that new particle formation on the scale of the grid box is unlikely. Accounting for anthropogenically produced sulfate particles in $N_a$ would imply the assumption of externally mixed aerosols, and hence an increase in sulfate would necessarily increase the number of cloud droplets. However, most combustion particles are internally mixed [see *Liousse et al.*, 1996, and references therein]. Therefore we assume that an internally mixed aerosol particle forms when sulfuric acid with continental origin condenses onto any preexisting aerosol particle; that is, anthropogenic sulfate only adds mass to the preexisting aerosols but does not form new aerosol particles.

The assumption of an internally mixed aerosol is included in the factor $\alpha$ in the above equations, which is derived from the results of a microphysical model [*Chuang et al.*, 1997]. If sulfuric acid condenses onto preexisting aerosol particles, they grow and become more hygroscopic and hence form cloud droplets at lower critical supersaturations. The value of $\alpha$ depends additionally on the geometric standard deviation of the initially preexisting lognormal aerosol size distribution, the mode radius, and the aerosol composition. It is parameterized as a function of updraft velocity $N_a$, and the mass of sulfate aerosols assuming internally mixed aerosols; $\alpha$ can range from $10^{-4}$ cm$^4$ s$^{-1}$ to 1 cm$^4$ s$^{-1}$. It is different for maritime aerosol spectrum and continental aerosol spectra:

$$\alpha^{\rm cont} = 0.041 + 21.59X_{\rm l} \quad (11)$$
$$\alpha^{\rm mar} = 0.022 - 0.13X_{\rm o} + 3.07X_{\rm o}^2 \quad (12)$$

where

$$X_{\rm l} = \frac{\log w(1 - \log w(0.5 + \gamma/\beta^4)/\log N_a^2)}{\log N_a^{\frac{5+\gamma}{\beta^3}}} \quad (13)$$
$$X_{\rm o} = \frac{\log w(1 - \log w(0.5 + 0.2\gamma/\beta^3)/\log N_a^2)}{\log N_a^{\frac{2+0.1\gamma}{\beta^2}}} \quad (14)$$

$\beta$ is the ratio of the local fraction of anthropogenic sulfate aerosols converted by the aqueous pathway to the mean value used by *Chuang et al.* [1997] of 0.75. Its interpretation is that if more sulfate is formed by gaseous phase production, more CCNs are activated than if more sulfate is formed within cloud droplets; $\gamma$ is referred to as the shape parameter for the sulfate-containing aerosol distribution and is defined as the ratio of anthropogenic sulfate loading ($\mu$g m$^{-3}$) to the total number of aerosol particles ($N_a$) (per 1000 cm$^{-3}$). The soluble material in the preexisting particles is assumed to have the same properties as ammonium sulfate. The anthropogenic sulfate-containing aerosol distributions produced through condensation and in-cloud oxidation should preserve their shape characteristics for given values of $\beta$ and $\gamma$. Different size distributions as described by *Chuang et al.* [1997] are applied to uniformly internally continental and marine aerosol particles, respectively. New evidence that those small particles can be activated is given by *Hallberg et al.* [1998]. To maintain the different size spectra of maritime and continental aerosol distributions when crossing the coastline, the final droplet nucleation rate is given as

$$Q_{\rm nucl} = \frac{Q_{\rm nucl}^{\rm cont} N_a^{\rm cont} + Q_{\rm nucl}^{\rm mar} N_a^{\rm mar}}{N_a} \quad (15)$$

The vertical velocity used for droplet nucleation is likely

to be underestimated in the free troposphere, because we consider its sub-grid-scale component from TKE alone, which peaks in the boundary layer. Thus the droplet nucleation in altostratus clouds would be underestimated. Therefore we assume a minimum of 40 cloud droplets $cm^{-3}$ to be always present. Even though some flight averages of droplet concentrations in marine clouds, for example over the Southern Ocean [*Yum et al.*, 1998], are below 40 $cm^{-3}$, the measurement uncertainties are large, so 40 $cm^{-3}$ is within one standard deviation and thus seems a reasonable assumption for clouds in a climate model.

In this study, different parameterizations for the evaporation of precipitation and sublimation of snow than in the work of *Lohmann and Roeckner* [1996] are used. Additionally sedimentation of ice crystals is considered here as well.

The parameterization of evaporation of rain and sublimation of snow used by *Lohmann and Roeckner* [1996] are only functions of relative humidity, while the ones used in this study are based on the rain rate and a ventilation factor or the snow rate. The parameterization of evaporation of rain is adapted from GESIMA [*Eppel et al.*, 1995] based on *Ogura and Takahashi* [1971]:

$$Q_{\mathrm{evr}} = \frac{1}{10^{-3}\rho} \frac{f_v(1 - q_v/q_{sl})(10^{-3}\rho q_r)^{0.525}}{4.1 \times 10^8/e_{sl} + 5.4 \times 10^5} \tag{16}$$

where $q_v$ is the water vapor, $q_{sl}$ is the saturation mixing ratio over liquid water, $q_r$ is the rainwater mixing ratio, $e_{sl}$ is the saturation vapor pressure, and $f_v$ is the ventilation factor, given as

$$f_v = 1.6 + 0.57\, v_r^{1.5} \tag{17}$$

where $v_r$ is the terminal fall velocity for raindrops [*Kessler*, 1969]:

$$v_r = 90.8 \left(\frac{\rho\, q_r}{n_{0r}}\right)^{0.125} \left(\frac{\rho_0}{\rho}\right)^{0.5} \tag{18}$$

where $n_{0r}=8 \times 10^6$ is the intercept parameter of the raindrop size distribution, and $\rho_0$ is a reference density ($=1.3$ kg $m^{-3}$).

The sublimation of snow is also adapted from GESIMA [*Levkov et al.*, 1992] based on *Lin et al.* [1983]:

$$Q_{\mathrm{sub}} = \frac{2\pi(1 - q_v/q_{si})}{\rho(A' + B')} n_{0s} \left(0.78\lambda_s^{-2} + 0.31 S_c^{0.33} \Gamma\left(\frac{b+5}{2}\right) \left(\frac{a}{\nu}\right)^{0.5} \left(\frac{\rho_0}{\rho}\right)^{0.25} \lambda_s^{(-b+5)/2}\right) \tag{19}$$

where $A' = L_s^2/(K_a R_v T^2)$, $B' = 1/(\rho q_{si} D_v)$, $\nu$ is the kinematic viscosity of air, $K_a$ is the thermal conductivity of air, $L_s$ is the latent heat of sublimation, $D_v$ is the diffusivity of vapor in the air, $S_c(=\nu/D_v)$ is the Schmidt number, $a$=4.83, and $b$=0.25.

Previously, aggregation of ice crystals and accretion of ice crystals with snowflakes were the only sinks for ice crystals due to precipitation. However, loss of ice crystals by sedimentation is an important sink as well, which is considered as follows:

$$Q_{\mathrm{falli}} = \frac{\partial}{\partial \eta}(q_i U_i) \tag{20}$$

where $q_i$ is the cloud ice-mixing ratio, and $U_i$ is the terminal velocity of pristine ice crystals [*Levkov et al.*, 1992], given as

$$U_i = a_i D_i \left(\frac{\rho_0}{\rho}\right)^{0.35} \tag{21}$$

where $a_i$=700 $s^{-1}$, and $D_i$ is the mean diameter of ice crystals which is given as a function of the cloud ice-mixing ratio as derived from observations around the British Isles [see *Lohmann and Roeckner*, 1996].

### 2.4. Optical Properties of Aerosol Particles and Cloud Droplets

Since the model provides only the spatial and temporal distribution of the mass of the different aerosol species, some assumptions about particle size distribution and chemical composition have to be made. At the moment we cannot compute optical properties of internally mixed aerosols, because not much is known of the optical properties of different internally mixed aerosols. Therefore we assume an external mixture of these aerosol compounds when calculating the aerosol optical depth. This is in contrast to droplet formation, where an internally mixed aerosol is assumed when anthropogenic sulfate is present. The assumption of externally mixed aerosols is correct near the sources of aerosols but not for aged aerosols. Findings from *Tang* [1996] show that this is justified for common hygroscopic aerosols where the chemical effect outweighs the size effect.

The aerosol mass mixing ratio of each species is transformed into a particle number concentration assuming a monomodal lognormal distribution with a prescribed mean particle radius. The optical properties, specific extinction, single-scattering albedo, and asymmetry factor are prescribed for every component, for different relative humidity classes, and spectral intervals. The optical and physical properties of the aerosol components used in this study and their dependency on the ambient relative humidity have been taken from *Köpke et al.* [1997] and are shown in Table 3.

Sulfate aerosols, either maritime or internally mixed continental aerosols, including OC, have physical properties suitable for a 75% sulfuric acid solution. These have a lognormal size distribution with a mode radius

**Table 3.** Aerosol Physical Properties: Mode Radius $r_m$ at 0% and 80% Relative Humidity (RH), Standard Deviation $\sigma$ of the Lognormal Distribution and Specific Density $\rho_s$ and Optical Aerosol Properties (Mass Extinction Efficiency $\sigma_e$, Single-Scattering Albedo $\omega_0$, and Asymmetry Factor $g$ for Dry Aerosols at 0.5 $\mu$m Wavelength)

| Aerosol Component | $r_m$ (0% RH) ($\mu$m) | $r_m$ (80% RH) ($\mu$m) | $\sigma$ ($\mu$m) | $\rho_s$ (g cm$^{-3}$) | $\sigma_e$ (m$^{-2}$ g$^{-1}$) | $\omega_0$ | $g$ |
|---|---|---|---|---|---|---|---|
| Sulfuric acid | 0.0695 | 0.118 | 2.03 | 1.7 | 3.80 | 1.00 | 0.77 |
| Water soluble | 0.0212 | 0.031 | 2.24 | 1.8 | 3.60 | 0.98 | 0.68 |
| Black carbon | 0.0118 | 0.012 | 2.00 | 1.0 | 11.00 | 0.23 | 0.35 |
| Dust | 0.3900 | 0.390 | 2.00 | 2.6 | 0.55 | 0.83 | 0.76 |
| sea-salt | 0.2090 | 0.416 | 2.03 | 2.2 | 1.30 | 1.00 | 0.78 |

According to *Köpke et al.* [1997].

of $r_m$=0.07 $\mu$m, a geometric standard deviation of 2.03, and a density of $\rho$=1700 kg m$^{-3}$. These values are used to transform the sulfate mass mixing ratio into particle number concentrations. Based on Mie-theory, the wavelength dependent optical parameters are calculated from their complex refractive indices and characteristic particle size distributions. The resulting mass scattering efficiency at a wavelength of 0.55 $\mu$m is 3.8 m$^2$ g$^{-1}$ for a 70% sulfuric acid solution at 0% relative humidity and changes with relative humidity. To consider the effects of organic carbon we use the aerosol properties as given for water soluble particles and for black carbon the properties of black carbon. The optical properties have been adapted to the model's spectral resolution by R. v. Dorland and I. Schult (unpublished results, 1997).

Dust and sea-salt aerosols are described above. Sea-salt and dust aerosols are assumed to be accumulation mode particles with a mode radius of 0.2 $\mu$m and 0.39 $\mu$m, respectively, when dry.

Growth of the particles due to water uptake has only been assumed for the hygroscopic aerosols, sulfate and sea-salt aerosols, and for the hydrophylic fraction of the organic carbon aerosols but not for black carbon, hydrophobic organic carbon, and dust. Sulfate aerosols, for instance, have a mode radius of 0.0695 $\mu$m at 0% relative humidity and 0.118 $\mu$m at 80% relative humidity.

The radiative properties of water droplets and approximately "equivalent" ice crystals are derived from Mie theory, and the results are fitted to the spectral bands of the radiation model and formulated in terms of cloud droplet and ice crystal effective radii [*Rockel et al.*, 1991]. For water clouds the effective radius of cloud droplets ($r_e$) is calculated from the cloud liquid water mixing ratio in the cloudy part of the grid box ($q_l/b$) and number of cloud droplets:

$$r_e = k\sqrt[3]{\frac{3\rho q_l}{4\pi b \rho_l N_l}} \tag{22}$$

where $k$=1.143 for continental clouds, and $k$=1.077 for marine clouds [*Johnson*, 1993] which accounts for the $\sim$ 10% larger effective radius than the mean volume radius, and $\rho_l$ is the density of water.

The effective ice crystal radius $r_i$ ($\mu$m) is an empirical function of cloud ice mixing ratio (S. Moss, personal communication, 1996):

$$r_i = 83.8 \times (10^3 \rho q_i)^{0.216} \tag{23}$$

## 3. Results

The results presented below are based on 5 year integrations at T30 resolution after a 3 months spin-up. The reference experiment was integrated over the 5 years using climatological sea surface temperatures. The sensitivity experiments were only integrated over 1 year after a spin-up of 3 months. The reference experiment is referred to as PROG to distinguish the prognostic treatment of the number of cloud droplets from the diagnostic treatment (DIAG) of the cloud droplet number concentration used by *Lohmann and Feichter* [1997].

### 3.1. Simulated Aerosol Distributions

The annual, global mean source strength (in Tg yr$^{-1}$), global burden (Tg) and aerosol optical depth of the individual species is given in Table 4. *Andreae* [1995] (hereinafter referred to as A95) compiled estimates of these quantities from the literature. His values are given for reference as well. Also included are the values obtained by *Tegen et al.* [1997] (hereinafter referred to as T97) using a chemical transport model. Sulfate burden and source strength are given in Tg S and Tg S yr$^{-1}$, respectively, and carbon burden and source strength in Tg C and Tg C yr$^{-1}$, respectively.

Our sulfur emissions are similar to other global sulfur cycle models [e.g., *Pham et al.*, 1995; *Chin et al.*, 1996] and A95. The sulfate burden is comparable to A95 and other sulfur cycle models [e.g., *Roelofs et al.*, 1998], as is its optical depth. It is twice as large as in T97, because in the *Chin et al.* [1996] model, which provided the monthly mean sulfate fields in T97, the scavenging is much larger than in the *Feichter et al.*

**Table 4.** Annual and Global Mean Source Strength, Burden and Aerosol Optical Thickness for Different Aerosol Species, Sulfate, Black Carbon, Organic Carbon, Soil Dust, and Sea-Salt

| Aerosol Component | Sulfate | BC | OC | Dust | Sea-Salt | Total |
|---|---|---|---|---|---|---|
| | | | *Source Strength* | | | |
| This study[a] | 95.5 | 11.7 | 105 | 106 | 76 | - |
| [*Andreae*, 1995][b] | 80.0 | 20.0 | 65 | 1500 | 1300 | - |
| [*Tegen et al.*, 1997][c] | 96.0 | 12.0 | 69 | 250 | 5900 | - |
| | | | *Burden* | | | |
| This study[a] | 1.00 | 0.26 | 1.87 | 2.2 | 0.7 | - |
| [*Andreae*, 1995][b] | 1.09 | 0.30 | 1.29 | 16.4 | 3.6 | - |
| [*Tegen et al.*, 1997][c] | 0.51 | 0.15 | 1.10 | 7.5 | 11.4 | - |
| | | | *Optical Depth* | | | |
| This study[a] | 0.064 | 0.002 | 0.021 | 0.002 | 0.009 | 0.098 |
| [*Andreae*, 1995][b] | 0.056 | 0.006 | 0.020 | 0.023 | 0.003 | 0.108 |
| [*Tegen et al.*, 1997][c] | 0.025 | 0.003 | 0.016 | 0.022 | 0.007 | 0.073 |

[a]Sea-salt and dust components refer to $r \leq 0.5$ $\mu$m.
[b]OC and sulfates are without biomass burning.
[c]OC is obtained from their carbonaceous aerosols minus BC. Their soil dust with $r < 1$ $\mu$m is quoted.

[1996] model. The source strength of BC is comparable to T97 but is smaller than in A95 because of differences from biomass burning. The source of BC and OC due to biomass burning is the same as in T97. The additional OC emissions are natural OC [*Guenther et al.*, 1995]. The BC optical depth is only a third of what was estimated in A95, but is similar to those reported in T97 calculated from *Liousse et al.* [1996], although our burden is much larger than in T97. Thus the specification of optical properties is very different in these studies. The optical depth of OC agrees very well with A95.

Our optical depth, burden, and source strength of dust are smaller than in A95 and T97, because our dust was scaled down to represent the fraction of $r < 0.5$ $\mu$m, whereas in A95, coarse mode particles are included, and the lowest size bin in T97 considers dust with $r < 1$ $\mu$m. However, our simulated optical depth is a factor of 10 lower than in T97, while the burden is only lower by a factor of 3, again a result of very different aerosol optical properties. The annual mean sea-salt burden amounts to 0.73 Tg, which is considerably lower than in T97 and A95. Compilation of an area-weighted sea-salt burden from measurements given by *Prospero* [1979] suggests a sea-salt burden of 4.1 Tg; that is, our sea-salt burden is much smaller than observations suggest, because we only consider sea-salt particles in the accumulation mode ($r < 1$ $\mu$m) in this study. Inclusion of the 1 - 10 $\mu$m mode gives a total of 5.5 Tg sea-salt. The global mean optical depth of sea-salt is 0.01, 3 times higher than in A95.

The globally averaged optical depth is 0.098 in very good agreement with A95 summarized from the aerosol contributions considered here. Two years of AVHRR (advanced very high resolution radiometer) measurements [*Husar et al.*, 1997] of aerosol optical thickness over the oceans suggest a global average of 0.12, 0.09 over the Southern Hemisphere (SH), and 0.15 over the Northern Hemisphere (NH). The contribution of the oceans in our study amounts to 0.07. The underestimation is likely to be caused by an underestimation of dust aerosols transported off the shore from the main deserts in this simulation.

In Figure 1 the annual mean burdens of sulfate aerosols, BC, OC, submicron diameter mineral dust and sea-salt, total aerosol depth from PROG and AVHRR, as well as the total number of aerosols ($N_a$) at 920 hPa are shown. Maxima in sulfate burden are associated with high sulfur emissions due to industrial activity in North America, Europe, and southeastern Asia. Secondary maxima in the Southern Hemisphere (SH) are due to biomass burning and smelting. The sulfate burden over SH oceanic regions is below 2 mg S $m^{-2}$. High levels of sulfate aerosols are transported downwind of the industrial centers off the shores of the Asian and North American coasts. Maxima over Indonesia and Kamchatka are due to volcanic emissions.

BC and OC have maxima over the industrial centers of Europe and southeastern Asia but not over the United States. BC and OC emissions are less over the United States than over Europe because not many cars burn diesel, which is responsible for the major anthro-

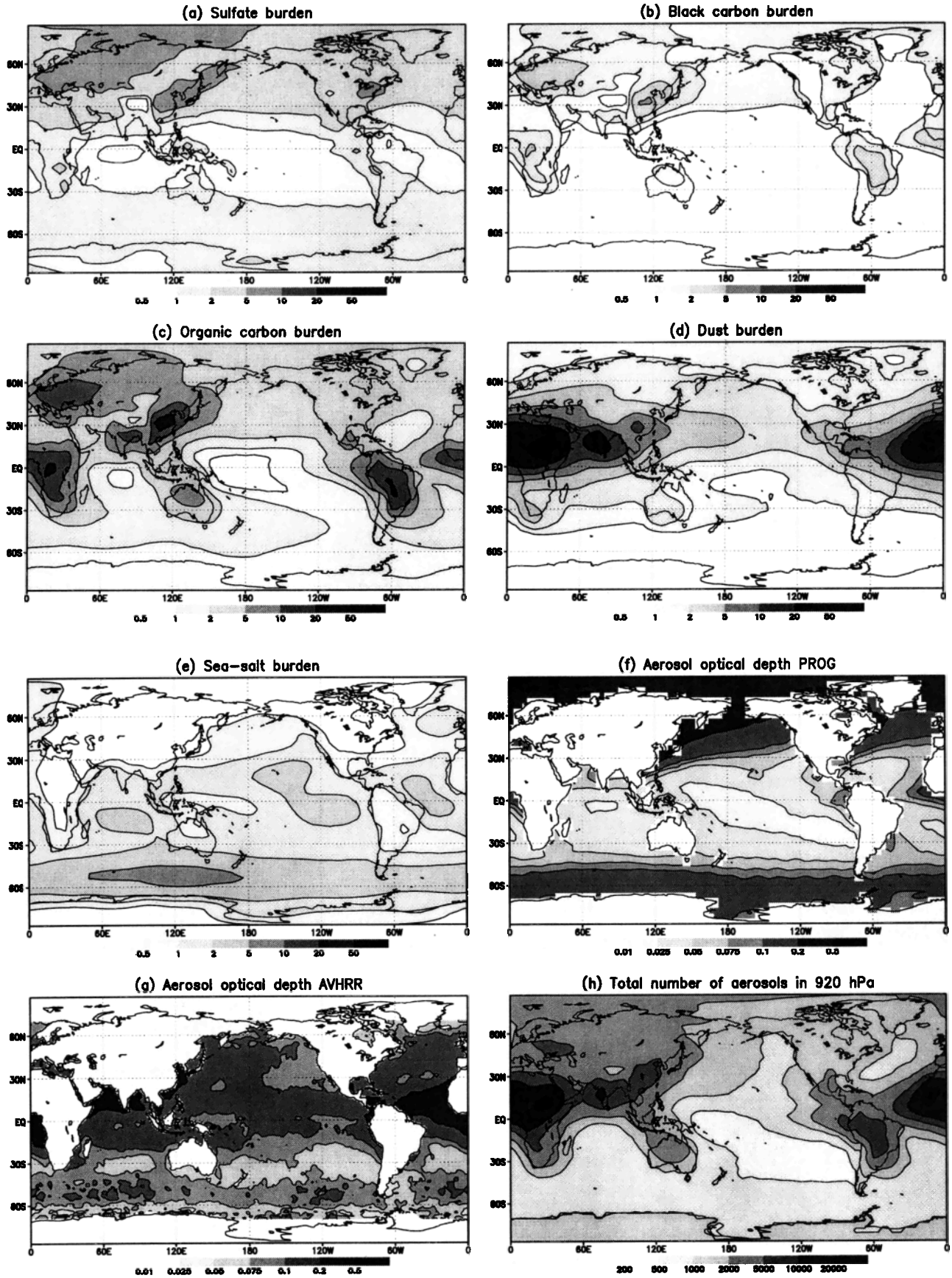


**Figure 1.** Annual mean burden of (a) sulfate (mg S $m^{-2}$), (b) black carbon (mg C $m^{-2}$), (c) organic carbon (mg C $m^{-2}$), (d) submicron dust (mg $m^{-2}$), (e) sea-salt (mg $m^{-2}$), (f) total aerosol optical depth from PROG, (g) aerosol optical depth from AVHRR, and (h) total number of aerosols in 920 hPa ($cm^{-3}$).

pogenic BC and OC emissions over Europe. However, BC and OC are underestimated over the United States by *Liousse et al.* [1996], which is the source of our data, as no biomass burning outside the tropics and subtropics is considered. Maxima on the Southern Hemisphere are caused by biomass burning.

The dust burden is largest over the Sahara, where the dust emissions are highest due to the combination of loose sand and high wind speeds. Saharan dust is transported as far as India and 300 km offshore the African continent eastward over the Atlantic. Sea-salt emissions, and thus its burden, also depend crucially on the wind speed. It is highest over the Southern Ocean with secondary maxima over all other oceans. Some sea-salt particles are transported over the continents as well.

AVHRR can only retrieve aerosol optical depth over oceans between 70°S and 70°N. It has maxima off the Saharan coast due to dust transport and off the coast of southeastern Asia and Africa closed to regions with large amounts of biomass burning. In PROG these maxima appear also, but the simulated optical depth is lower than observed (Figures 1f and 1g). The simulated aerosol optical depth agrees in magnitude with the observed one in midlatitudes but is too low in the tropics. This suggests the need for simulating sea-salt and dust from the model-generated winds rather than offline with monthly mean winds. However, this is beyond the scope of the present paper but will be addressed in the future.

$N_a$ is shown at 920 hPa, which is the nearest level to the total number of aerosol particles shown by *Chuang et al.* [1997, Plate 1]. *Chuang et al.* [1997] find the most aerosols over Europe, southeastern Asia, and Brasilia when using the same internal mixing approach as used here. Our total number of aerosol particles is largest over the Sahara, primarily because of the inclusion of dust aerosols, whereas *Chuang et al.* [1997] only considered OC, BC, and sulfates. South America has more aerosols than North America, which is a reflection of the OC and BC distributions which, however, unrealistically neglect biomass burning outside the tropics where it is not so effective. Most of the emissions over North America occur on the east coast, where the particles are rapidly transported over the Atlantic. Also, the assumption that all anthropogenic sulfate condenses onto preexisting particles is an extreme, while in reality, some anthropogenic sulfates form new aerosol particles. Some dust is transported over the oceans, so the land/sea contrast in total number of aerosol particles is only a factor of 3, with 5900 aerosols $cm^{-3}$, on average, over land and 1800 aerosols $cm^{-3}$ over oceans. *Jaenicke* [1993] suggests number concentrations for maritime aerosols between 100 and 900 $cm^{-3}$ and for continental aerosols between 2000 and 8000 $cm^{-3}$ at that altitude, which implies that our aerosol number concentrations are on the high side. At the same time, our aerosol optical depth is smaller than in AVHRR. Thus either our specific extinction coefficients are too small or there is a contradiction in those estimates from observations.

### 3.2. Simulated Cloud Distributions

**3.2.1. Global Means.** Table 5 shows a comparison of globally averaged values of the simulated liquid water path, cloud cover, and the shortwave cloud forcing for summer and winter obtained from PROG and DIAG with observations. Additionally, we present the hemispheric mean effective radius for warm clouds (cloud top temperature > 273.2 K) separately for maritime and continental clouds. The effective radius is calculated as the satellite would see it; that is, it corresponds to the radius at cloud top.

The estimates for liquid water path from special sensor microwave imager (SSM/I) observations over oceans cover the period 1987-1991 [*Greenwald et al.*, 1993] and 1987-1994 [*Weng and Grody*, 1994]. The accuracy of the retrieved liquid water path from microwave emissions over ice free oceans is still rather low, and the retrievals can be affected by many input factors (e.g., total precipitable water, surface wind, cloud tem-

**Table 5.** Liquid Water Path (LWP), Cloud Cover (CC), Shortwave Cloud Forcing (SCF), Longwave Cloud Forcing (LCF), and Cloud Droplet Effective Radius $r_e$ for NH Winter (DJF) and NH Summer (JJA)

| Quantity | OBS (DJF) | PROG | DIAG | OBS (JJA) | PROG | DIAG |
|---|---|---|---|---|---|---|
| Liquid water path (g $m^{-2}$)[a] | 48.0-75.4 | 92.1 | 90.8 | 49.5-76.7 | 92.4 | 82.0 |
| Cloud cover (%) | 61.5 | 67.8 | 61.8 | 62.1 | 64.6 | 57.7 |
| Shortwave cloud forcing (W $m^{-2}$) | -52.4 | -49.7 | -55.7 | -48.3 | -43.4 | -47.8 |
| Longwave cloud forcing (W $m^{-2}$) | 28.7 | 27.1 | 30.5 | 29.1 | 28.3 | 30.3 |
| $r_e$ SH oceans ($\mu$m)[b] | 11.6 | 11.6 | | 11.6 | 11.9 | |
| $r_e$ NH oceans ($\mu$m) | 10.2 | 11.4 | | 12.2 | 11.3 | |
| $r_e$ SH land ($\mu$m) | 9.0 | 10.0 | | 9.3 | 8.1 | |
| $r_e$ NH land ($\mu$m) | 7.8 | 5.0 | | 9.0 | 8.4 | |

[a]Only data over oceans equatorward of 60° are considered. The lower value in the SSM/I observations corresponds to the estimate by *Weng and Grody* [1994] and the higher value to *Greenwald et al.* [1993].
[b]Only data equatorward of 50° are considered.

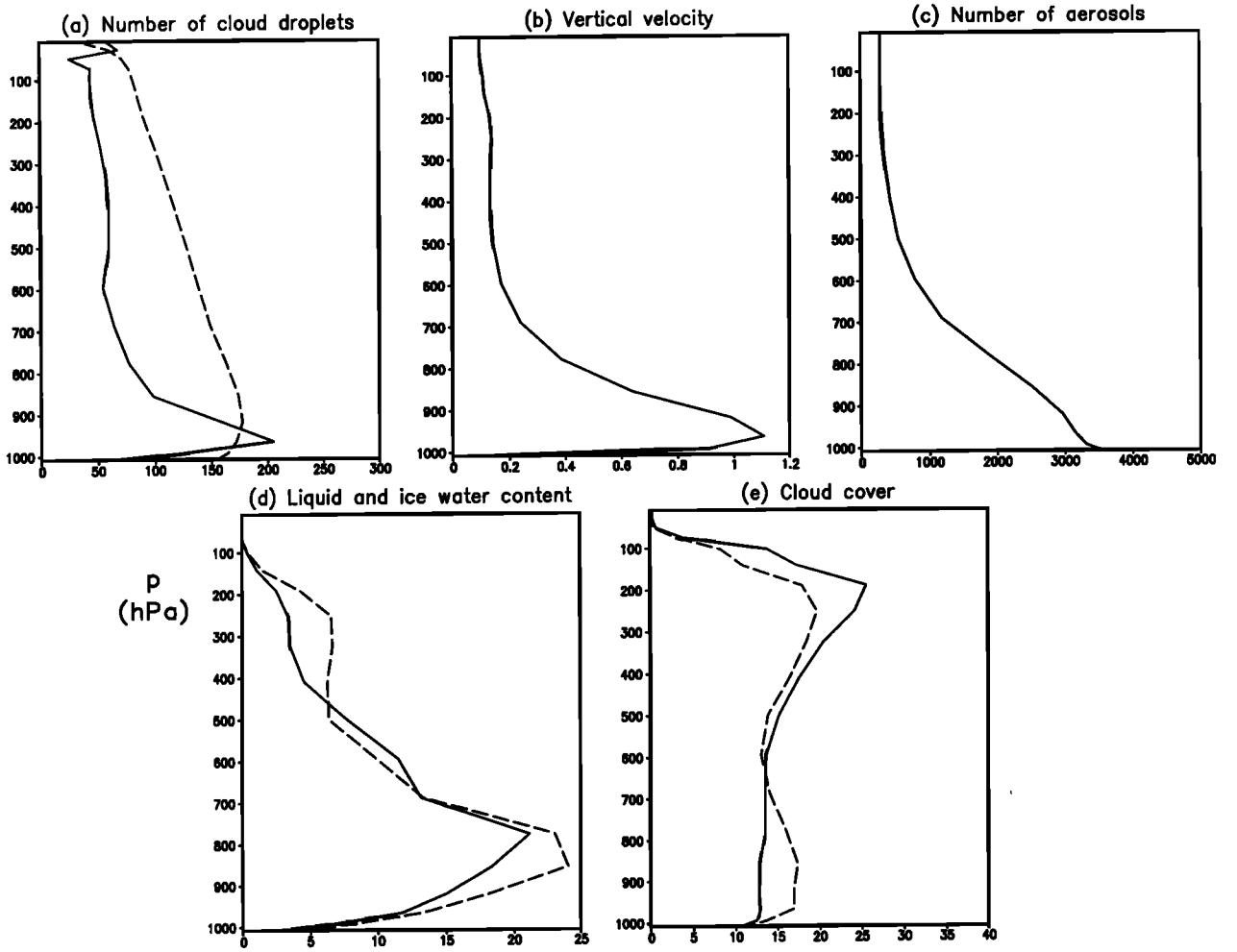


**Figure 2.** Annual global mean vertical profiles for PROG (solid) and DIAG (dashed) of (a) the number of cloud droplets ($cm^{-3}$), (b) vertical velocity (m $s^{-1}$), (c) the total number of aerosol particles ($cm^{-3}$), (d) sum of liquid and ice water content (mg $kg^{-1}$), and (e) cloud cover (%).

perature). There are also possible contributions from precipitation-size drops in the retrieved liquid water path. Hence the retrievals from *Greenwald et al.* [1993] and *Weng and Grody* [1994] differ regionally by a factor of 2 and in the global annual mean by 60%. Both data sets are used for their pattern in the first place and as an estimate of the possible range of liquid water path in the second place. Observed total cloud cover, averaged over 1983-1990, and the effective cloud droplet radius are derived from the International Satellite Cloud Climatology Project (ISCCP) [*Rossow and Schiffer*, 1991; *Han et al.*, 1994]. The observations of shortwave and longwave cloud forcing are obtained from ERBE, averaged over the years 1985-1990.

The simulated global mean liquid water path is higher than derived from SSM/I data by *Greenwald et al.* [1993] and thus much higher than estimated by *Weng and Grody* [1994], but the change with season simulating slightly higher values in JJA is captured. The cloud cover is 10% higher than observed in NH winter and 4% higher in NH summer. The higher cloud cover in PROG than in DIAG can be attributed to the large-scale transport of cloud water and cloud ice, which was neglected in DIAG. The semi-Lagrangian scheme applied for advection is numerically quite diffusive and changes therefore the vertical humidity structure. Thus the vertical mixing is too strong, which results in a higher cirrus cloud cover. Therefore we had to enhance the aggregation rate to readjust our longwave cloud forcing again to the observed one from ERBE. The shortwave cloud forcing is underestimated by 2.7 W $m^{-2}$ in NH winter, and 5 W $m^{-2}$ in NH summer, both of which are within the range of measurement uncertainty. The longwave cloud forcing is within $\pm$ 2 W $m^{-2}$ of the observations in both seasons.

The simulated effective radii are within 1 $\mu$m for marine clouds and continental clouds over the Southern Hemisphere. We underpredict the effective radii for continental clouds in NH winter by 3 $\mu$m caused by either a too low liquid water content or a higher CDNC. The latter could result from too many CCN being activated in PROG. This point will be discussed further

in section 3.2.3. The simulated land-sea contrast is 3.9 $\mu$m, slightly higher than the 3.3 $\mu$m derived from the ISCCP [*Han et al.*, 1994]. The observations show that the effective radii over SH oceans are 0.6 $\mu$m larger than over NH oceans, whereas the difference is only 0.3 $\mu$m in PROG. This is very likely caused by the inherent assumption of a uniform maritime aerosol spectrum with a volume-mean radius of 0.085 $\mu$m, whereas in situations with high wind speed and large amounts of sea salt in the marine boundary layer, the volume-mean radius could be larger.

The slightly higher than observed liquid water path and cloud cover should yield a shortwave cloud forcing that is larger than observed rather than smaller. To understand the apparent contradiction, the liquid water path, cloud cover, and shortwave cloud forcing from *Lohmann and Feichter* [1997], using the empirical relationship between sulfate aerosols and the number of cloud droplets, are included in Table 5 as well (experiment DIAG). In DIAG the liquid water path and cloud cover are lower than in PROG, but the shortwave cloud forcing is higher. Thus the differences are either due to a different vertical distribution of cloud cover, liquid water, and the number of cloud droplets in those experiments or due to differences in spatial and temporal variability. As shown in Figure 2, the vertical profile of the CDNC in DIAG is much smoother than in PROG, even though we mimic cloud dynamics by assuming that the same number of cloud droplets which is nucleated at cloud base prevails throughout the depth of the cloud. In the extratropics, clouds are frequently layered, so more than one cloud base exists in a vertical GCM column. Thus the number of drops that nucleate is much lower for an altostratus cloud as compared to a stratus cloud as the number of aerosol particles and the vertical velocity rapidly decrease with height (compare Figure 2). The number of aerosol particles decreases from 3500 $cm^{-3}$ near the surface to 300 $cm^{-3}$ above near the tropopause. The values in the boundary layer are representative for a remote continental aerosol as compiled by *Jaenicke* [1993] and thus are probably too high for a global mean average. Also the decrease with height is not so rapid as suggested by *Jaenicke* [1993], so the number of aerosol particles in the free atmosphere in PROG is larger than observed as well. However, by comparing CDNC between DIAG and PROG, one needs to have in mind that CDNC is a hypothetical number in DIAG as it is linked to the mass of sulfate aerosols that are always present. In PROG CDNCs are only produced when condensation occurs and are subject to loss by evaporation and precipitation formation. In addition, the higher temporal and spatial variability of the number of cloud droplets in the prognostic approach may also account for the apparent inconsistency among liquid water path, effective radius, and shortwave cloud forcing.

The cloud water content (sum of liquid and ice) and cloud cover are higher in DIAG than in PROG below 700 hPa. Additionally, for clouds with tops higher than 900 hPa on average, the number of cloud droplets is larger in DIAG, thus the effective cloud droplet radius is smaller, and more shortwave radiation is reflected back to space. The cirrus cloud cover is lower in DIAG, but its water content is higher yielding a similar longwave cloud forcing (compare Table 5).

**3.2.2. Cross sections.** Figure 3 shows cross sections of $N_a$, the ratio of the mass of anthropogenic sulfate aerosols to $N_a$ ($\gamma$), which is one parameter that determines the factor $\alpha$ in equation (9), CDNC, the vertical velocity, the liquid water content in the cloudy part of the grid-box and averaged over cloudy events only (in-cloud liquid water content), and the precipitation efficiency for warm clouds (defined as the ratio of precipitation formation in mixing ratio units to the in-cloud liquid water content).

$N_a$ is largest at 20°N, predominantly due to high aerosol number concentrations of dust over the Sahara. It rapidly decreases with height until it reaches the background concentration of 300 particles $cm^{-3}$.

The ratio of anthropogenic sulfate aerosols to $N_a$ is largest over middle and high latitudes of the Northern Hemisphere reflecting the main sources of anthropogenic sulfate. It is relatively constant with height as many anthropogenic sulfate aerosols are formed by gas-to-particle conversion and via the aqueous pathway far away from the origin of their precursors. This ratio exhibits a strong latitudinal gradient, it decreases sharply from above 3.5 north of 45°N to below 1 at 15°N, reflecting again the latitudinal gradient of anthropogenic aerosol sources.

CDNC has maxima below 900 hPa in the tropics where the vertical velocity and $N_a$ are highest, i.e., where most aerosols can be activated. Between 900 and 700 hPa it decreases rapidly with height, much faster than $N_a$ and the number of aerosol particles. Both CDNC and $N_a$ decrease poleward and exhibit a secondary maximum near 50°S.

The in-cloud liquid water content also has maxima in the tropics with values up to 0.5 g $kg^{-1}$ between 900 hPa and 700 hPa associated with shallow convection. These clouds convert, on average, 40% of their liquid water content into precipitation, distinctly less than clouds formed over the Intertropical Convergence Zone. The precipitation efficiency is highest for clouds formed near the surface, where the in-cloud liquid water content is depleted very rapidly. It's maximum in the Intertropical Convergence Zone and over the storm tracks corresponds to a relative minimum in in-cloud liquid water content and relatively low number of cloud droplets. Altostratus clouds and polar clouds precipitate less efficiently.

The distribution of the in-cloud liquid water content is much smoother than the one of the cloud droplet number. The condensed cloud liquid water is calculated with a saturation adjustment scheme. It depends only on the supersaturation, which is controlled by large-

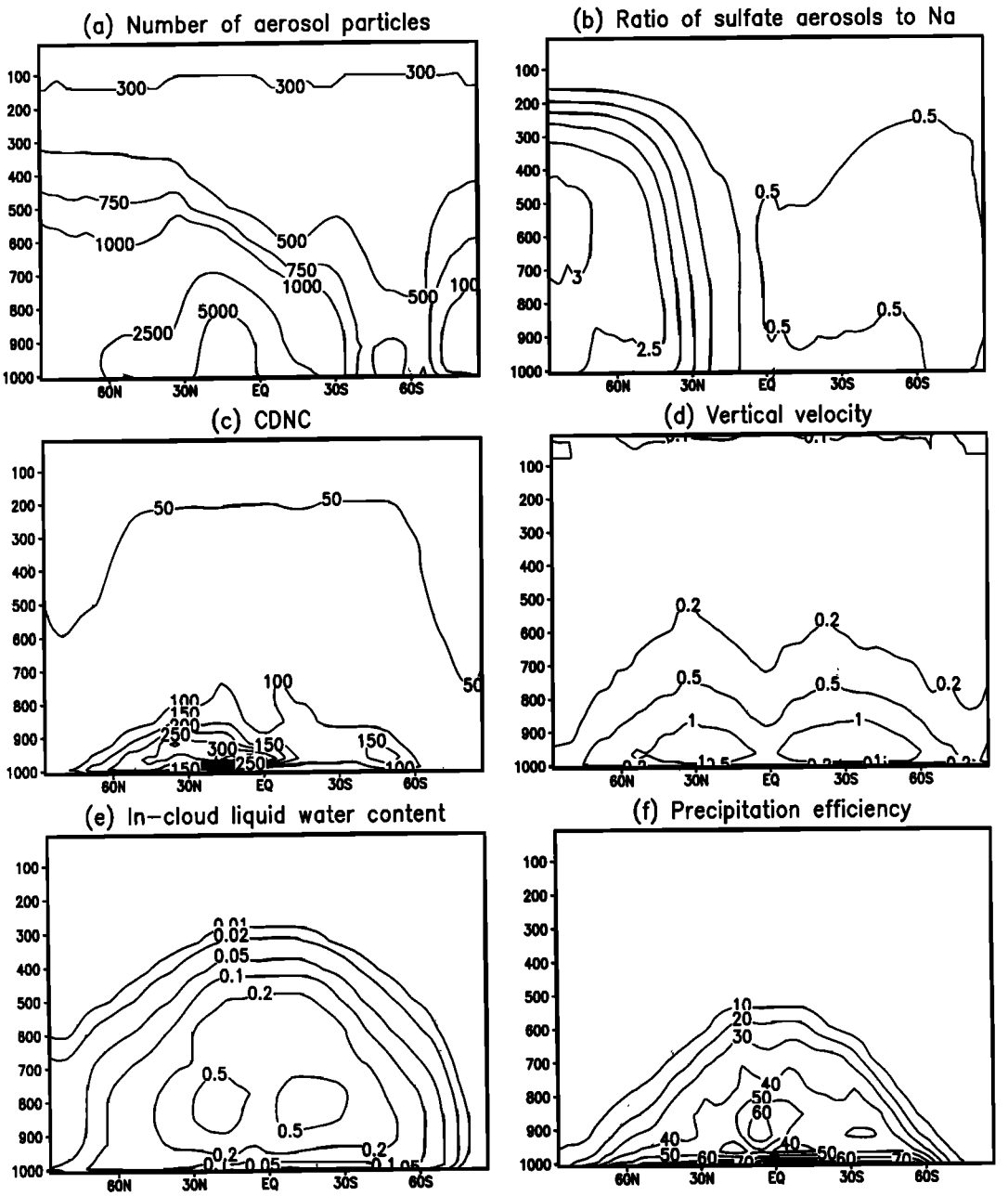


**Figure 3.** Annual zonal mean latitude-pressure (hPa) cross sections of (a) total number of aerosol particles ($cm^{-3}$), (b) ratio of anthropogenic sulfate to the total number of aerosol particles ($\gamma$) ($\mu g\ m^{-3}\ S/1000\ cm^{-3}$), (c) CDNC ($cm^{-3}$), (d) vertical velocity ($m\ s^{-1}$), (e) in-cloud liquid water content ($mg\ kg^{-1}$), and (f) precipitation efficiency (%).

scale dynamics. The activation of cloud droplets, however, is controlled by the turbulent vertical velocity fluctuation rather than by the grid-mean vertical velocity, so the cloud droplet number concentration is more noisy.

**3.2.3. Geographical distributions.** The annual mean conversion rates for CDNC and CDNC itself in 920 hPa averaged over clear-sky and cloudy areas are shown in Figure 4. Similar to *Ghan et al.* [1997], nucleation in large-scale clouds is the major source with $3.7 \times 10^6\ m^{-2}\ s^{-1}$. Maxima are found over Europe, off the Saharan coast, and in East Africa. Minima are generally located in high-pressure areas of the subtropics and over North America and eastern Asia. Detrainment from convective anvils is a much smaller source with $1.1 \times 10^6\ m^{-2}\ s^{-1}$ in the global mean. It has maxima in the tropics due to shallow convection. Detrainment from deep convection is only a minor source, because most of its detrained cloud water occurs in the ice phase. Advection and diffusion are negligible as is melting of cloud ice. The largest sink is evaporation of cloud droplets similar to the findings of *Ghan et*

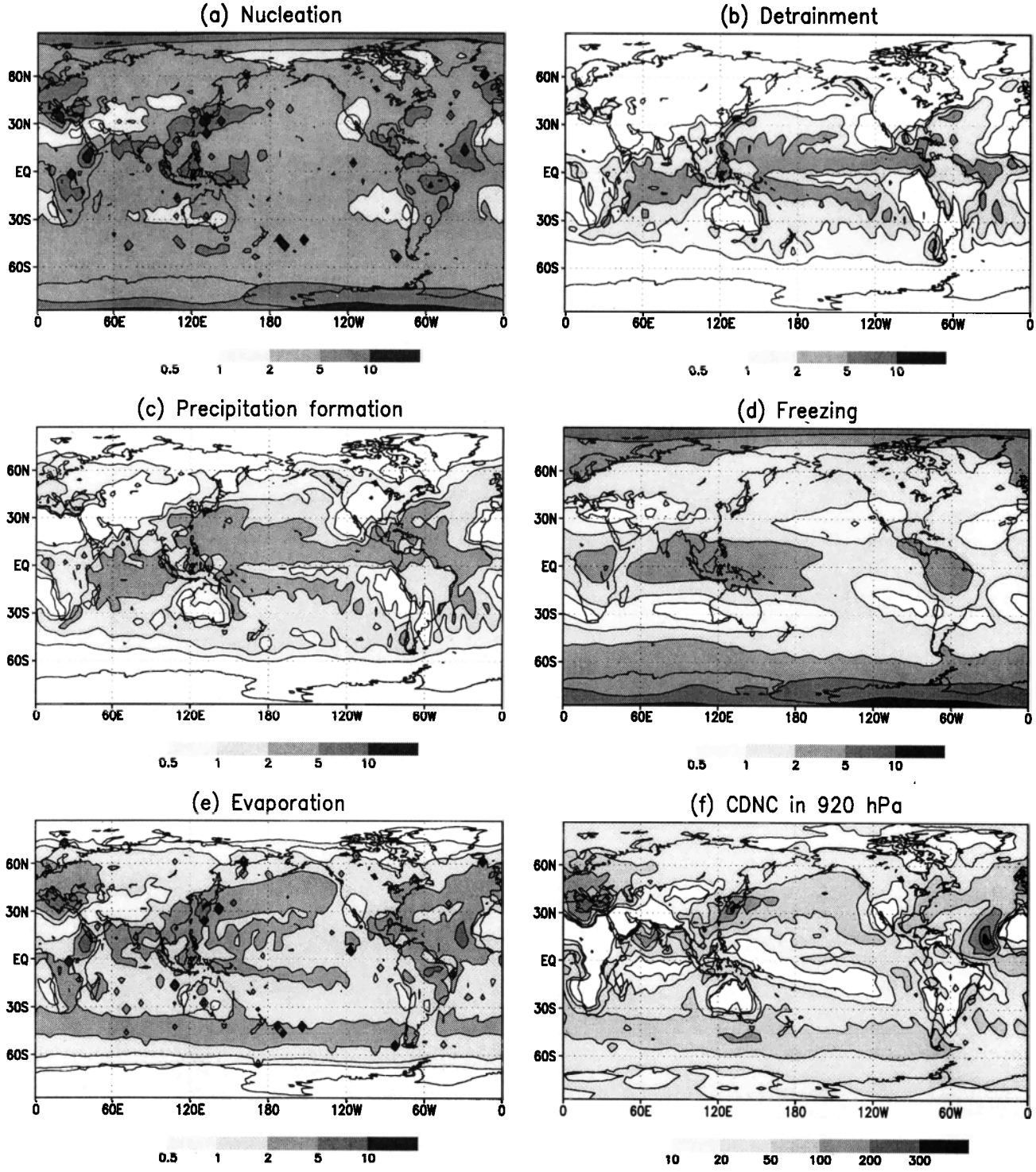


**Figure 4.** Annual mean vertically integrated sources and sinks for the number of cloud droplets ($10^{-6}$ m$^{-2}$ s$^{-1}$): (a) nucleation, (b) detrainment from convective anvils, (c) precipitation formation, (d) freezing, (e) evaporation, and (f) and the number of cloud droplets itself (cm$^{-3}$) in 920 hPa.

*al.* [1997] with $1.9 \times 10^6$ m$^{-2}$ s$^{-1}$ in the global mean followed by freezing of cloud droplets ($1.7 \times 10^6$ m$^{-2}$ s$^{-1}$) and precipitation formation ($1.2 \times 10^6$ m$^{-2}$ s$^{-1}$). Precipitation formation exhibits a similar geographical distribution as detrainment, whereas freezing is largest near the poles and in areas of deep convective activity. Evaporation is largest off the Saharan and east Asian coast and nearly uniform elsewhere.

The resulting distribution of CDNC (Figure 4f) shows much more small-scale features than the number of aerosol particles in this level (compare Figure 1). Maxima are located over the storm tracks of each hemi-

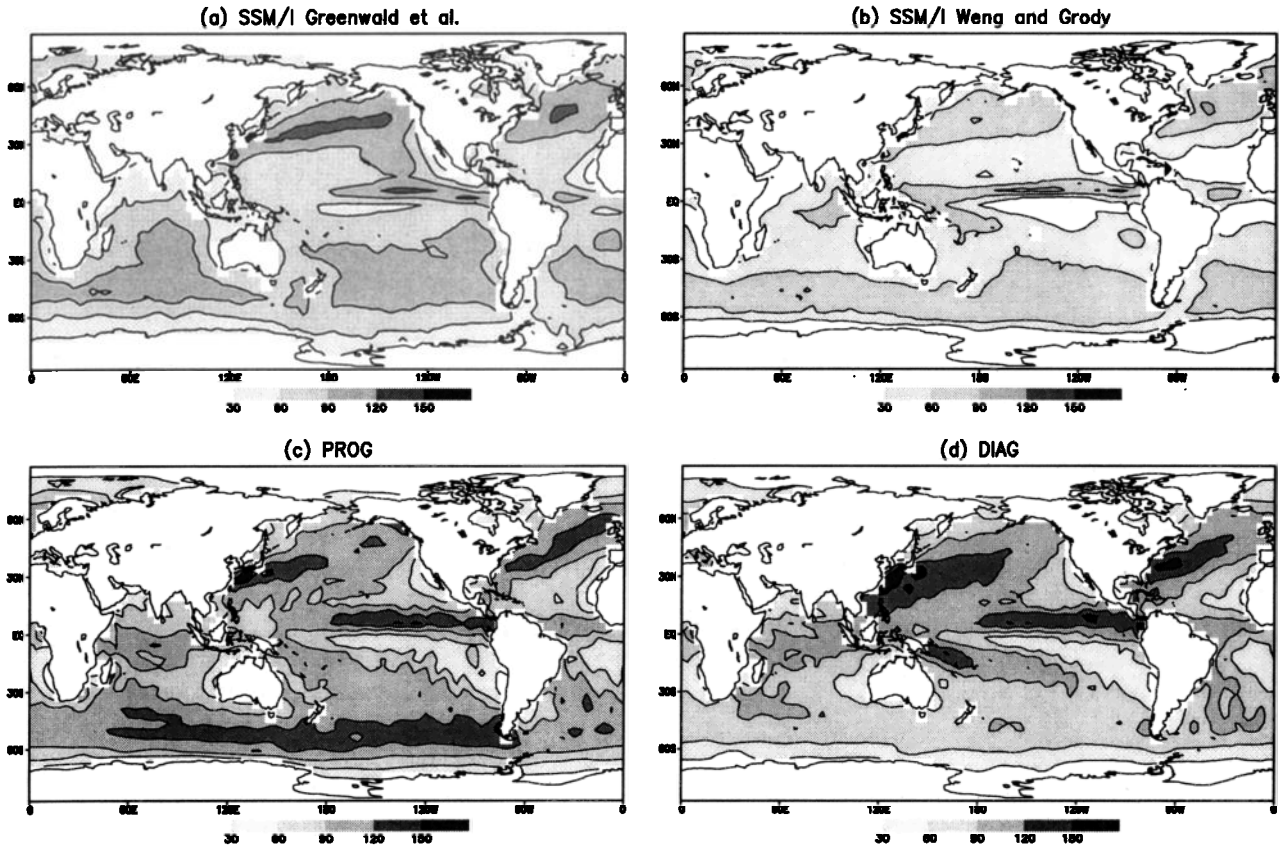


**Figure 5.** Geographical distribution of the annual mean liquid water path (g $m^{-2}$) obtained from (a) SSM/I analyses according to *Greenwald et al.* [1993], (b) according to *Weng and Grody* [1994], (c) PROG, and (d) DIAG.

sphere as well as over Europe off the Saharan coast. Lower concentrations are generally found over the continents and over the southern Pacific where few aerosols are present (compare Figure 1). In the stratocumulus regions off the west coasts of North America and South America, the droplet concentration is between 50 and 100 $cm^{-3}$.

The annual mean liquid water path is shown in Figure 5. PROG and DIAG capture the observed maxima in liquid water path associated with tropical convection and NH extratropical cyclones. In PROG the liquid water path over SH oceans is higher than the observations suggest. However, the zonal pattern shows a maximum at 50°S and a distinct minimum over SH subtropics similar to the observations from *Weng and Grody* [1994], whereas in DIAG the liquid water path is not much higher at 50°S than in SH subtropics. In both experiments, the convectively active regions in the tropics are more pronounced than in the observations. Because of high levels of anthropogenic aerosols and hence high concentration of cloud droplets in DIAG, higher values of liquid water path than observed are predicted over the western part of the North Atlantic and North Pacific. This overestimation, especially in the Pacific between 10°N and 20°N, is nicely reduced in PROG.

The annual and zonal mean cloud droplet effective radii for warm clouds with cloud top temperatures > 273.2 K between 50°N and 50°S from PROG and observations from *Han et al.* [1994] are presented in Figure 6. In both the observations and PROG the largest difference between maritime and continental effective cloud droplet radii occurs in the subtropics. The agreement between simulated and observed effective radii is best in the tropics. Larger departures from the observations occur over land in the Northern Hemisphere north of 15°N and over midlatitude oceans, where the simulated radii are too small. As the liquid water path in PROG is not underpredicted in NH midlatitude storm tracks with respect to SSM/I observations (compare Figure 5), the simulated clouds probably consist of too many CDNC. A comparison of column CDNC for low-level clouds with cloud top temperature > 273.2 K from ISCCP data [*Han et al.*, 1998b] for a 1 year mean (taken as average over January, April, July, and October 1987) and PROG for a 1 year mean (also composed of a January, April, July, and October) suggests that the latter is true (Figure 7). In general, the agreement of annual mean column CDNC simulated with PROG and derived from ISCCP is very good. Column CDNC is on average much higher over land than over the oceans

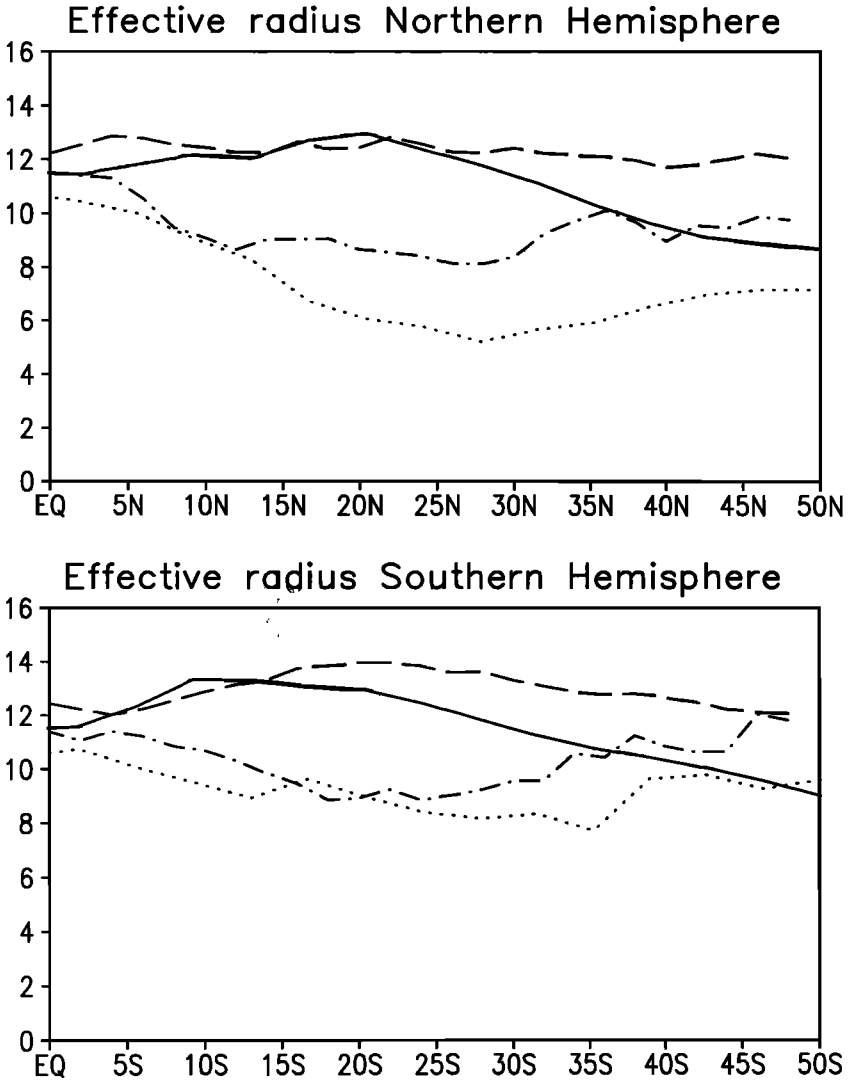


**Figure 6.** Annual mean cloud droplet effective radius ($\mu$m) for (top) the Northern Hemisphere and (bottom) Southern Hemisphere for observations over oceans (dashed), over land (dotted-dashed) and PROG over oceans (solid) and over land (dotted).

both in observations and in PROG. *Han et al.* [199b] emphasized the striking difference in contrast between maritime and continental clouds such that continental clouds consist of 2-4 times more cloud droplets than maritime clouds. A comparison of frequencies of cloud droplet concentration for clouds over land and ocean is shown in Figure 8. Observations show that more than 80% of low-level clouds over oceans in all seasons have column droplet concentration $< 4 \times 10^6$ cm$^{-2}$ while only 30% of clouds over land. In ECHAM the frequency distribution of column droplet concentration of maritime clouds is captured very well, but the land-sea contrast is much smaller. The regional distribution of column droplet concentration (Figure 7) yields that the largest deviation from observations is in coastal regions, where PROG predicts too high values. PROG generally underpredicts clouds in the interior of the continents, so even over land the maximum in frequency is in the lowest bin. However, one has to bear in mind that ISCCP has difficulties in distinguishing CDNC from dust aerosols over the Sahara which could bias the observed frequency distribution to larger column CDNC.

*Han et al.* [1998a] addressed the point of the relationship of cloud albedo and liquid water path with droplet size. As shown in Figure 9, the interesting finding is that only for optically thick clouds ($\tau > 15$) and for clouds over land the cloud albedo (and optical depth) increase with decreasing droplet size, which is the underlying assumption for the indirect aerosol effect. For optically thinner clouds ($\tau < 15$) the time available for droplet growth leads to an increase in liquid water path and cloud albedo with increasing droplet size. For all warm clouds the liquid water path increases with increasing effective radius as to be expected in the droplet growth state where CDNC is almost constant. This opposite behavior for optically thin and thick clouds over

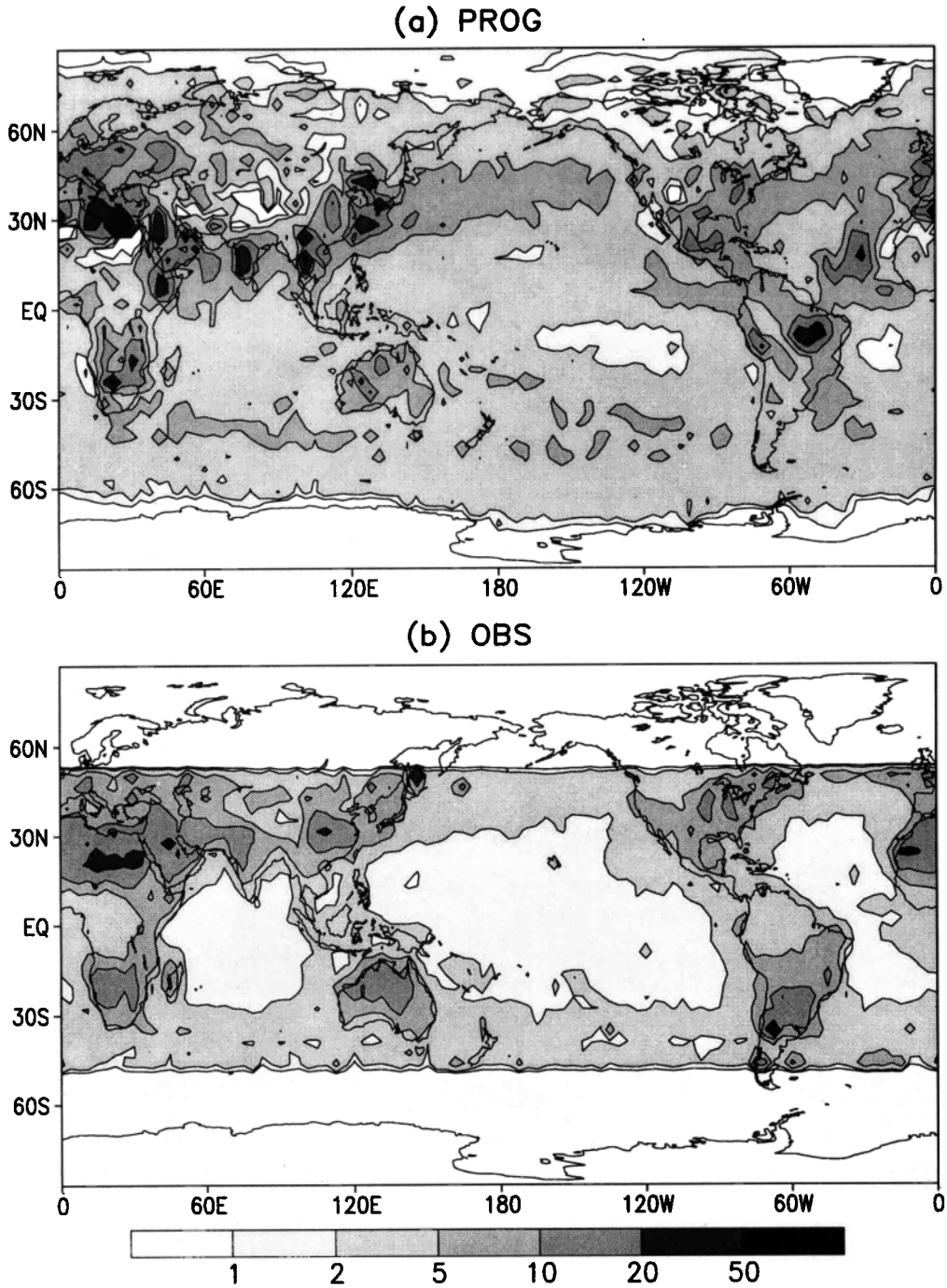


**Figure 7.** Geographic distribution of the annual mean column cloud droplet number concentration ($10^6$ cm$^{-2}$) from (a) PROG, and (b) ISCCP.

the oceans is captured in PROG (Figure 9). However, the land-sea contrast for optically thin clouds is not simulated; that is, optically thin clouds over land behave like optically thin clouds over oceans in PROG, whereas they behave like optically thick clouds in ISCCP.

The influence of clouds on the shortwave radiation, the shortwave cloud forcing, is shown in Figure 10 for PROG and DIAG together with satellite observations from ERBE. In agreement with ERBE data, maxima in shortwave cloud forcing occur where maxima in liquid water path are located (e.g., over tropical convectively active regions, NH storm tracks, and SH oceans). Secondary maxima are associated with marine stratocumulus decks offshore of the coasts of California and South America. Although both DIAG and PROG capture the main features, the shortwave cloud forcing in the tropics is overestimated in DIAG, especially over the warm pool and underestimated in extratropical cyclones with respect to ERBE. In PROG the shortwave cloud forcing is increased in the extratropics of the Southern Hemi-

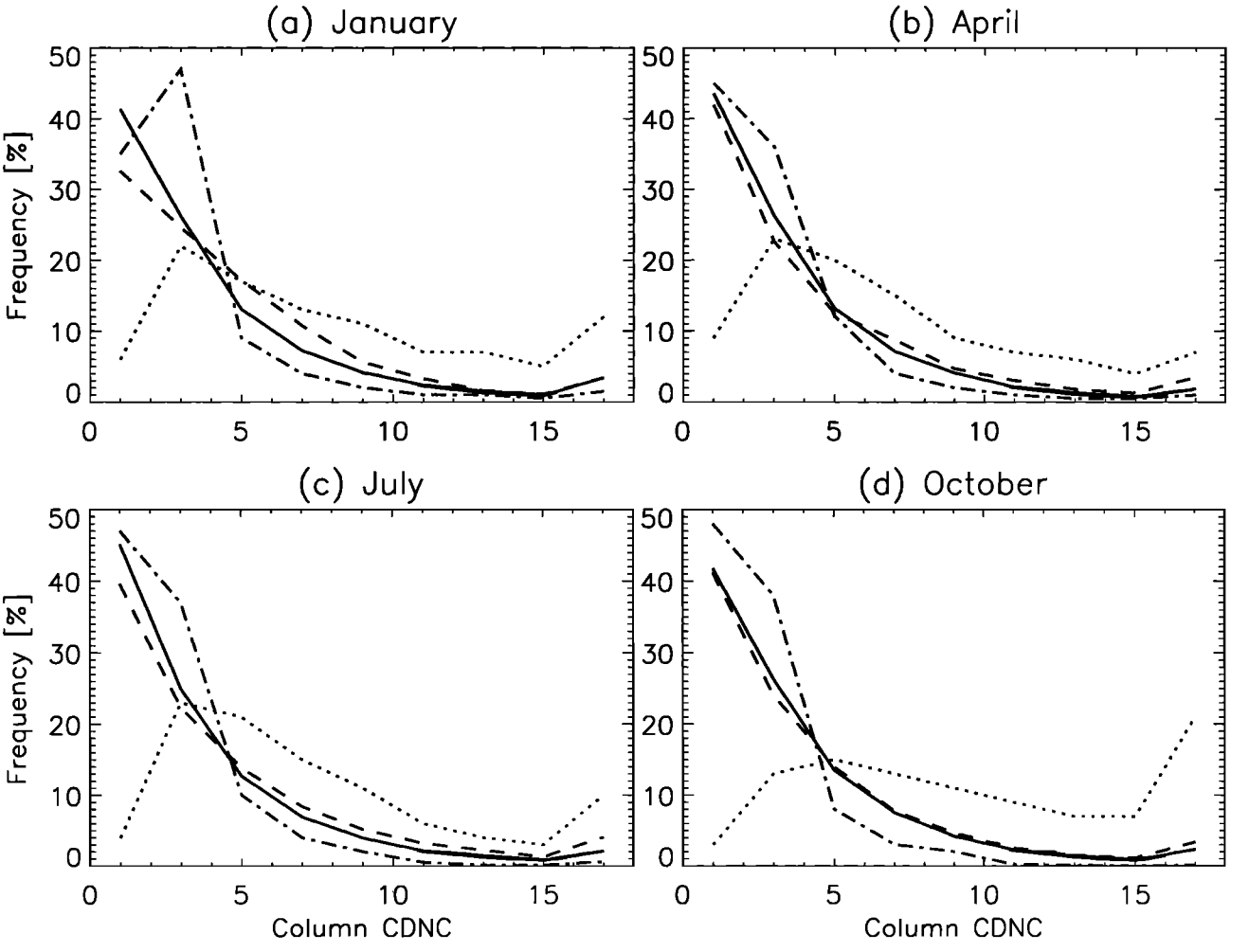


**Figure 8.** Frequency distribution of column cloud droplet number concentration ($10^6$ cm$^{-2}$) for (a) January, (b) April, (c) July, and (d) October from PROG for clouds over land (dashed), over oceans (solid) and from ISCCP [*Han et al.*, 1998b] for clouds over land (dotted), over oceans (dotted-dashed).

sphere, and reduced in the tropics, in better agreement with the ERBE data. Moreover, the minimum in shortwave cloud forcing over the subtropical highs is nicely captured. As can be clearly seen in the zonal mean (Figure 10d), the good agreement of the global mean shortwave cloud forcing in DIAG compared to ERBE is partly due to error compensation, the shortwave cloud forcing being overestimated in the tropics and underestimated in the extratropics. In PROG the agreement of the shortwave cloud forcing is excellent everywhere but on the Northern Hemisphere, where probably the assumption that anthropogenic sulfate never forms new aerosol particles is not correct.

To summarize, the experiment with the prognostic treatment of cloud droplets simulates a liquid water path and a shortwave cloud forcing which is in closer agreement with the observations than the experiment with the empirical relationship between the mass of sulfate aerosols and CDNC. This is mainly due to additional aerosols such as sea-salt over the Southern Ocean and a different vertical profile of CDNC in those two experiments. The average column CDNC of marine clouds is realistically simulated except over NH extratropical storm tracks where very large column CDNC cause a lower effective radius than observed. Very encouraging, the changes in effective radius with optical depth, which is different for optically thin and thick marine clouds, is captured in PROG.

## 4. Sensitivity Experiments

Aerosol activation is highly sensitive to the maximum supersaturation, which is related to the updraft velocity and the chemical composition, size, and number of aerosol particles. In this section, sensitivity experiments are conducted, changing the input parameter of the nucleation parameterization, i.e., the total number of aerosol particles, the vertical velocity, and the value of $\alpha$, which contains the information about the aerosol composition, size spectrum, and hygroscopicity. The sensitivity experiments are summarized in Table 6.

In the first two experiments, the factor $\alpha$ is varied. In

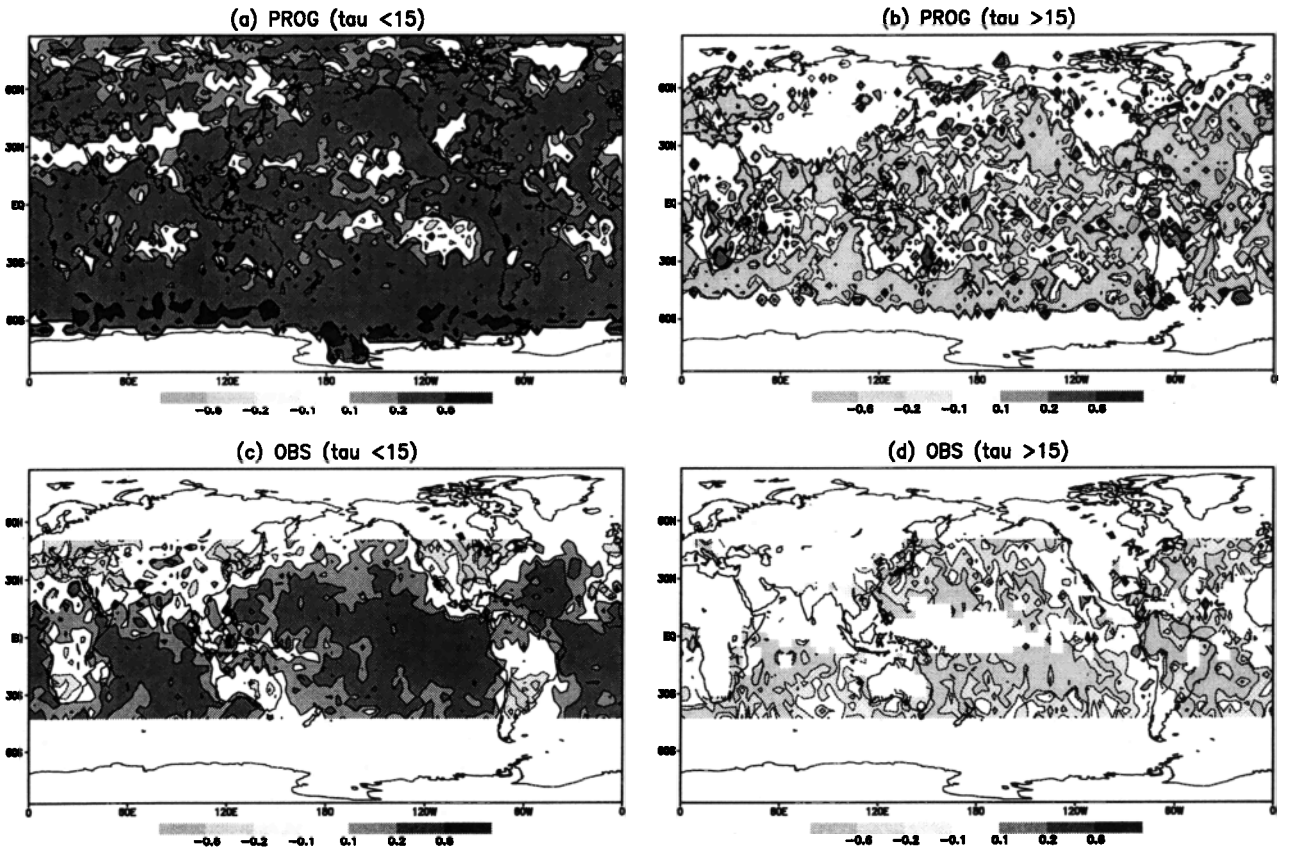


**Figure 9.** Geographic distribution of the correlation coefficient of effective radius and optical depth obtained from PROG (a) for optical thin clouds ($\tau < 15$), (b) for optical thick clouds ($\tau > 15$), and the correlation coefficient of effective radius and cloud albedo obtained from ISCCP [*Han et al.*, 1998a] for (c) optical thin clouds ($\tau < 15$), and (d) for optical thick clouds ($\tau > 15$).

PROG it is assumed that the maritime aerosol spectrum is conserved when advected over land and vice versa for the continental aerosol spectrum. The sensitivity to the conservation of size spectrum is studied in the experiment $\alpha$-la/oc, where $\alpha$ changes its character as soon as air masses cross the coastline. In $\alpha$-Ghan we use an averaged value of $3.4 \times 10^{-3}$ cm$^4$ s$^{-1}$ for the factor $\alpha$, as given by *Ghan et al.* [1993], valid for ammonium sulfate, assuming a lognormal size distribution with a mode radius of 0.05 $\mu$m and $\sigma$=2 at 800 hPa and 273 K.

To test the sensitivity of the droplet activation to the total number of aerosols, we conducted two experiments, one where we used 2000 aerosols cm$^{-3}$ everywhere close to the average number of aerosol particles obtained with PROG over the oceans at 920 hPa. In the other experiment we distinguish maritime and continental aerosols as simply as possible by assuming that continental air contains 5000 aerosols cm$^{-3}$ and maritime air 800 aerosols cm$^{-3}$.

The sensitivity to aerosol activation to updraft velocity suggests that the number of nucleated cloud droplets could be highly sensitive to the way which we specify vertical velocity. We conducted two sensitivity experiments, one where we prescribe a vertical velocity of 10 cm s$^{-1}$ everywhere and one where we use a vertical velocity of 1 m s$^{-1}$. These numbers are a good estimation of a lower and upper bound for typical values found in stratus clouds [*Gultepe and Isaac,* 1996].

As summarized in Table 7, in PROG $\sim$ 1800 aerosols cm$^{-3}$ prevail, on average, over the oceans at 920 hPa, and we predict about 150 cloud droplets cm$^{-3}$. Over land, more than 3 times as many aerosols are present in this altitude, but only 50% more cloud droplets exist in the global mean, because the nucleation of cloud droplets becomes rapidly saturated over land at a high number of aerosols. The in-cloud liquid water content at 920 hPa over the oceans is 50% higher than over land; the annual mean cloud cover at 920 hPa over the oceans is 14% as compared to 9% over land, and the precipitation efficiency is 40% over oceans, 4% higher than over land.

### 4.1. Sensitivity to $\alpha$

The results hardly change if no transport of the maritime aerosol spectrum over land and of the continental aerosol spectrum over the oceans is considered, as in

**Table 6.** Sensitivity Experiments

| Abbreviation | Description |
|---|---|
| $\alpha$-la/oc | aerosol size distribution changes immediately as air masses cross the coastline |
| $\alpha$-Ghan | a constant $\alpha$ value of $3.4 \times 10^{-3}$ cm$^4$ s$^{-1}$ is used |
| $N_a$-uni | $N_a$ is assumed to be 2000 cm$^{-3}$ everywhere |
| $N_a$-la/oc | $N_a$ is assumed to be 800 cm$^{-3}$ over the oceans and 5000 cm$^{-3}$ over land |
| W-small | vertical velocity is 10 cm s$^{-1}$ everywhere |
| W-large | vertical velocity is 100 cm s$^{-1}$ everywhere |

$\alpha$-la/oc. Neglecting the transport should increase the number of cloud droplets over land as the number of cloud droplets nucleated is not weighted by the amount of maritime aerosols present. Conversely, fewer cloud droplets should be present over the oceans. However, the number of cloud droplets has decreased over oceans and over land. CDNC has decreased over land because the number of new CDNC formed levels off very fast with increasing number of aerosols. The increase in liquid water path is 1% compared to PROG as the areal increase in the number of cloud droplets outweighs its decrease (Figure 11). The largest increase in the number of cloud droplets occurs in the subtropics. As the precipitation efficiency decreases when the cloud consists of more but smaller cloud droplets, the lifetime of those clouds is prolonged, and on average, more liquid water is present, mainly collocated with the increase in cloud droplets, as can be seen in Figure 11.

If no aerosol properties are included in the factor $\alpha$, but a constant value as in $\alpha$-Ghan is used, than the number of cloud droplets is about twice as large in 920 hPa than in PROG, both over land and over oceans (Table 7). This is a result from activating more aerosols here, which reduces the precipitation efficiency of these clouds and thus enhance their lifetime. As shown in Figure 11, the increase in cloud droplet number concentration and liquid water content prevail everywhere below 500 hPa. Thus the liquid water path is increased by 9 g m$^{-2}$, and the shortwave cloud forcing is highest in this experiment. Even though the increase in liquid water path is 12% in $\alpha$-Ghan, as compared to PROG, the increase in shortwave cloud forcing is only 1%. Firstly, this is due to overlying high and midlevel clouds which have not changed. Secondly, if the low-level clouds are already optically thick, a further increase in cloud droplets and liquid water path, on average, hardly increases the shortwave cloud forcing.

### 4.2. Sensitivity to Number of Aerosol Particles

Using an average aerosol concentration of 5000 cm$^{-3}$ over land and 800 cm$^{-3}$ over oceans everywhere, as in $N_a$-la/oc, changes the vertical distribution of aerosols drastically. In 920 hPa, fewer aerosols, on average, are present in this experiment over the oceans than in PROG (Table 7). The total number of particles is reduced between 20°S and 30°N below 700 hPa and increased elsewhere (not shown). The smallest increase occurs over the Southern Ocean in higher altitudes. CDNCs decrease below 700 hPa between 50°N and 10°S as a result from fewer CCN, and thus the faster collision-coalescence process depletes the liquid water content of these clouds more rapidly (Figure 12). Vice versa, the larger amount of aerosols above 700 hPa results in more CDNC and longer-lasting midlevel clouds, so that the liquid water path only decreases by 3% and the short-

**Table 7.** Annual Means of Total Number of Aerosol Particles $N_a$, Number of in-Cloud Cloud Droplets (CDNC), and in-Cloud Liquid Water Content (LWC) at 920 hPa, Annual and Global Mean LWP, and SCF for Sensitivity Studies

| Quantity | PROG | $\alpha$-la/oc | $\alpha$-Ghan | $N_a$-la/oc | $N_a$-uni | W-Small | W-Large |
|---|---|---|---|---|---|---|---|
| $N_a$-ocean (cm$^{-3}$) | 1801 | 1767 | 1782 | 800 | 2000 | 1804 | 1823 |
| $N_a$-land (cm$^{-3}$) | 5910 | 5861 | 5916 | 5000 | 2000 | 5962 | 5956 |
| CDNC-ocean (cm$^{-3}$) | 154 | 165 | 307 | 128 | 219 | 67 | 125 |
| CDNC-land (cm$^{-3}$) | 224 | 188 | 529 | 200 | 162 | 69 | 164 |
| LWC-ocean (mg kg$^{-1}$) | 243 | 249 | 293 | 248 | 274 | 210 | 255 |
| LWC-land (mg kg$^{-1}$) | 160 | 160 | 173 | 159 | 162 | 138 | 165 |
| LWP (g m$^{-2}$) | 77.2 | 78.2 | 86.4 | 78.6 | 81.7 | 73.3 | 80.6 |
| SCF (W m$^{-2}$) | -46.3 | -46.3 | -46.8 | -46.3 | -46.6 | -45.4 | -46.4 |

See Table 6

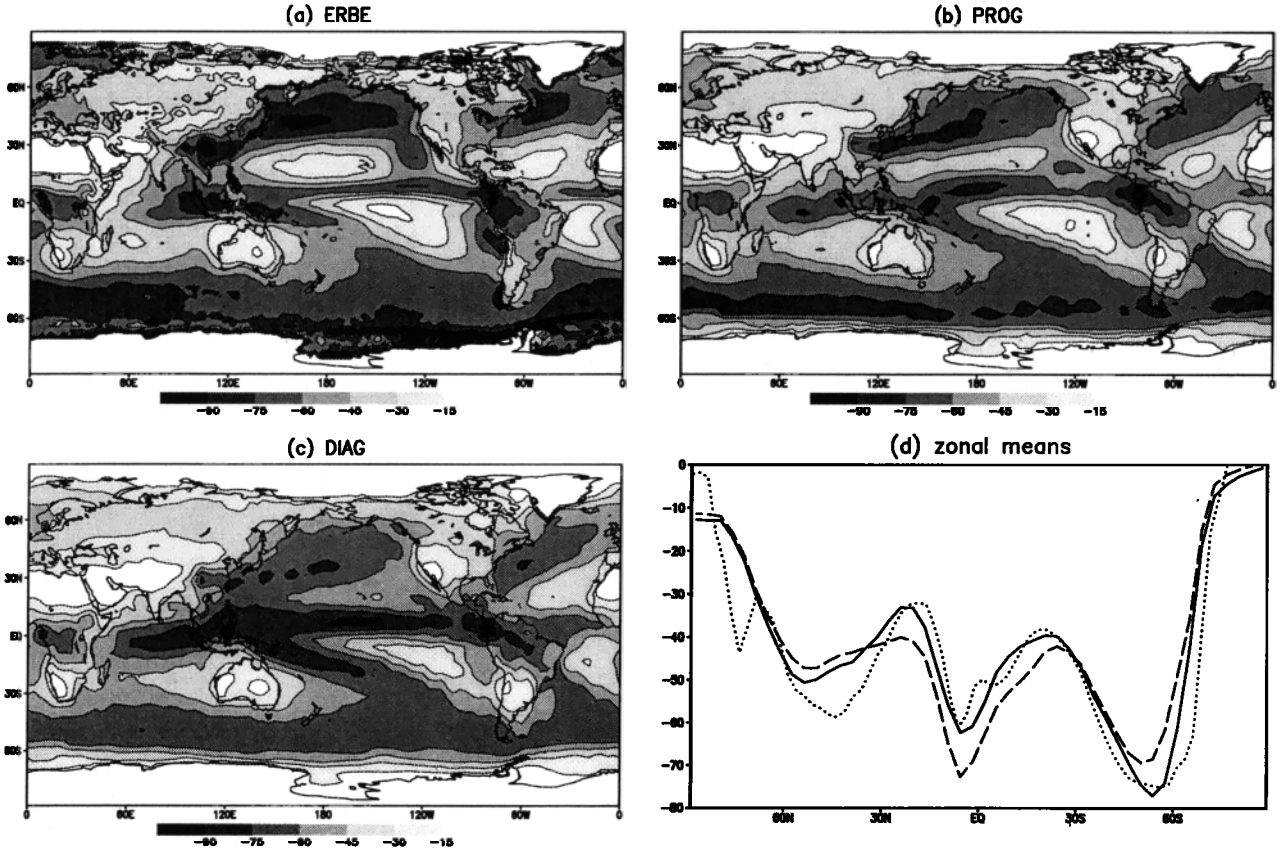


**Figure 10.** Geographic distribution of the annual mean shortwave cloud forcing (W $m^{-2}$) obtained from (a) ERBE, (b) PROG, (c) DIAG, and (d) zonal annual mean shortwave cloud forcing from ERBE (dotted), PROG (solid), and DIAG (dashed).

wave cloud forcing reduces by 1 W $m^{-2}$. The ratio of anthropogenic sulfate to the total number of aerosol particles, $\gamma$, decreases poleward of 40°N and increases south of it (not shown); that is, in this scenario the anthropogenic aerosols add mass onto preexisting aerosol more evenly. More CDNC prevail over the Southern Ocean and north of 50°N, where using our simulated aerosols less than 800 aerosol $cm^{-3}$ prevail. The liquid water content shows a dipole structure decreasing by more than 20 mg $kg^{-1}$ in the Northern Hemisphere and increasing by more than 50 mg $kg^{-1}$ in the Southern Hemisphere, so the liquid water path increases by 1.4 g $m^{-2}$. The positive and negative changes cancel each other, yielding the same shortwave cloud forcing as in PROG.

Assuming 2000 aerosols $cm^{-3}$ everywhere as in $N_a$-uni reduces the total number of particles between 20°S and 60°N below 700 hPa and increases the total number of particles elsewhere (not shown). The number of CDNC in 920 hPa is higher over ocean than over land in this experiment, the reversed of what is simulated with PROG (Table 7); that is, the assumption of different size spectra over land and ocean is very crucial for the number of activated CCN. In the zonal mean, CDNCs have increased almost everywhere on the Southern Hemisphere and poleward of 30°N and decreased between the equator and 30°N (Figure 12). Here the decrease over tropical and subtropical land masses outweighs the increase over tropical oceans. The in-cloud liquid water content has increased everywhere, with maxima of more than 100 mg $kg^{-1}$ in the subtropics of both hemispheres. This results in a 6% increase in liquid water path as compared to PROG.

### 4.3. Sensitivity to Vertical Velocity

The sensitivity of CDNC to small changes in the vertical velocity was found to be small [*Chuang et al.*, 1997; *Ghan et al.*, 1997]. Here we evaluate the changes in CDNC using an upper and lower bound of typical values of vertical velocity. If the vertical velocity is only 10 cm $s^{-1}$ everywhere (experiment W-small), the number of cloud droplets is reduced to 70 $cm^{-3}$ both over land and over ocean, which is 2 and 3 times smaller than in PROG in 920 hPa over land and ocean, respectively. The number of cloud droplets is reduced everywhere, with a maximum reduction of more than 100 $cm^{-3}$ in the boundary layer between 60°N and 10°S, as can be seen in Figure 13. Thus the in-cloud liquid water content is reduced everywhere below 700 hPa as well. The

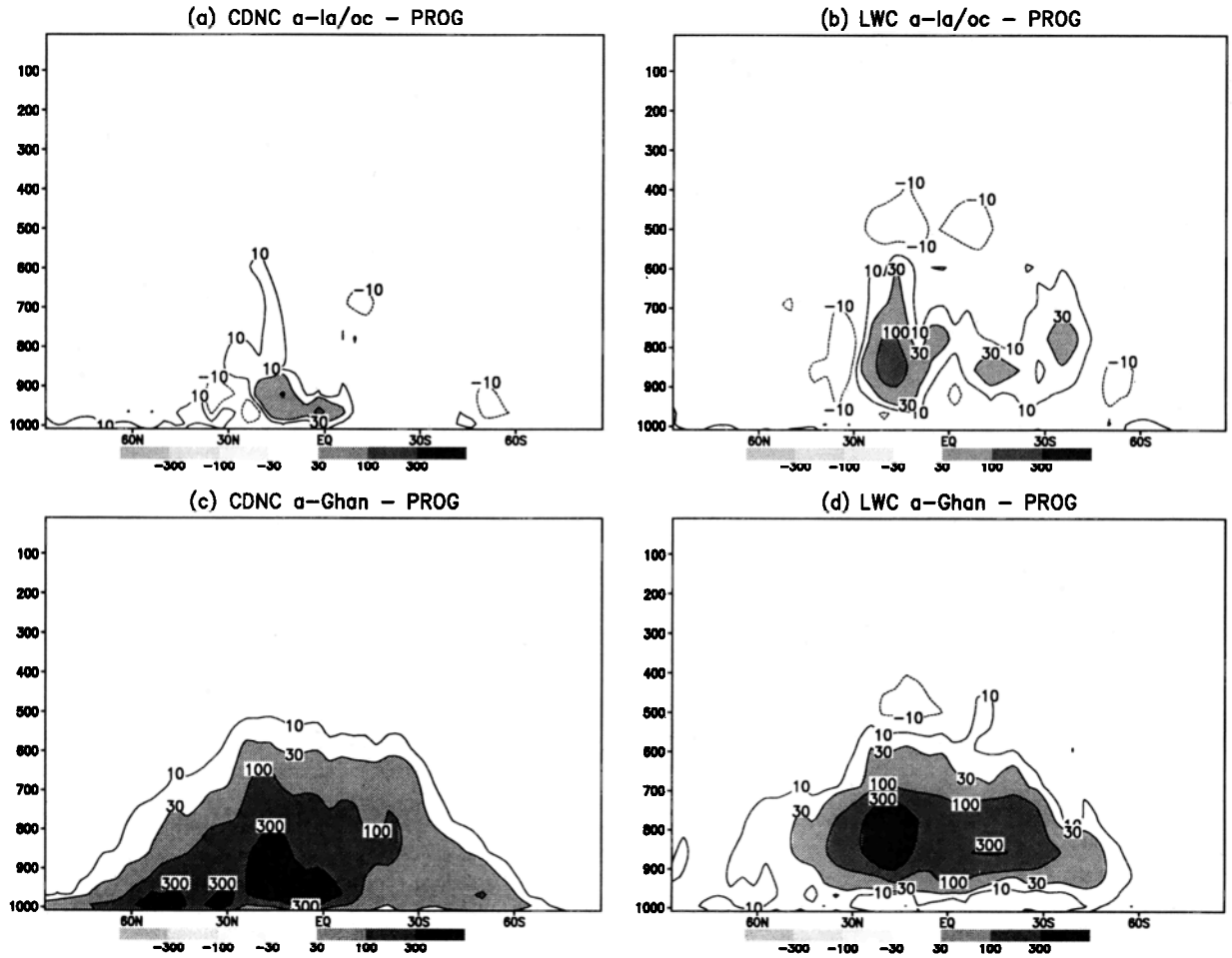


**Figure 11.** Annual zonal mean latitude-pressure (hPa) cross sections of the differences between sensitivity experiment $\alpha$-la/oc and PROG for (a) CDNC ($cm^{-3}$), (b) in-cloud liquid water content (mg $kg^{-1}$), and difference between the sensitivity experiment $\alpha$-Ghan and PROG for (c) CDNC ($cm^{-3}$), and (d) in-cloud liquid water content (mg $kg^{-1}$).

boundary layer clouds convert slightly more cloud water into precipitation, which increases the annual global mean precipitation by 0.5%. As a result of the lower cloud water content, the liquid water path is 3.9 g $m^{-2}$ lower in this experiment than in PROG, and the shortwave cloud forcing is lowest in this experiment, 0.9 W $m^{-2}$ lower than in PROG.

Assuming a vertical velocity of 1 m $s^{-1}$ everywhere does not give the opposite picture, because the vertical velocity below 900 hPa exceeds 1 m $s^{-1}$ in PROG. As in W-small, in this experiment the number of cloud droplets in 920 hPa is lower than in PROG (compare Table 7), but the in-cloud liquid water content is higher, as compared to PROG. As the vertical velocity drops below 1 m $s^{-1}$ above 900 hPa in PROG, the liquid water content and the number of cloud droplets in W-large are increased above that level, and the precipitation efficiency is reduced, as can be seen in Figure 13. Overall, the increase in liquid water content in W-large, as compared to PROG, outweighs the decrease, so the liquid water path is increased in the global mean. The shortwave cloud forcing, however, is not larger in W-large than in PROG, because the decrease in the number of cloud droplets below 850 hPa reduces the optical depth of the boundary clouds more than its increase aloft increases the optical depths of the midlevel clouds.

The differences in liquid water path and shortwave cloud forcing between these sensitivity experiments and PROG are small, because many of the cloud processes are dynamically controlled rather than by their microphysical properties. The dynamics are pretty similar, as neither the precipitation nor the longwave cloud forcing, which would be a good indicator for changes in the dynamics, differ much between those experiments. In all experiments both quantities are within ± 1% of the global mean values in PROG and do not exhibit large regional deviations either.

To summarize, the smallest changes occur when the aerosol size distribution changes immediately as air masses cross the coastline, as compared to transports

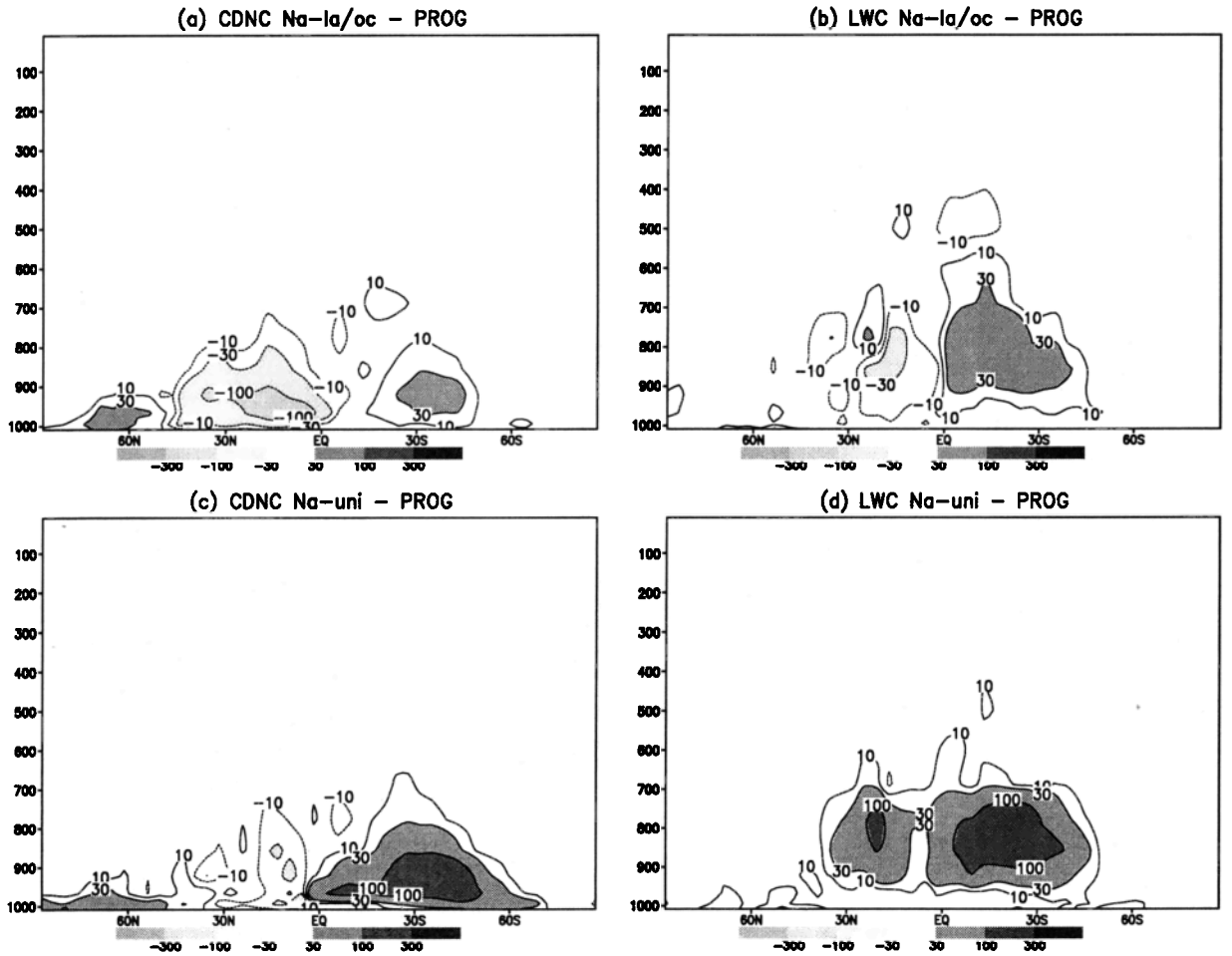


**Figure 12.** As Figure 11 but for the difference between sensitivity experiments $N_a$-la/oc and PROG and between $N_a$-uni and PROG.

of the size distribution. On the contrary, the liquid water content changes regionally by more than 0.1 g kg$^{-1}$ when a constant value of $\alpha$ is used, when a constant number of aerosol particles is assumed, or the vertical velocity is 1 m s$^{-1}$ everywhere.

## 5. Discussion and Conclusions

In this paper we introduce a prognostic equation for the number of cloud droplets (experiment PROG) into the ECHAM GCM. With that we are able to estimate the number of cloud droplets from solving a budget equation, which is more physically sound than relating it diagnostically to the mass of sulfate aerosols which is taken as a surrogate for the total aerosol mass. The implied assumption in the diagnostic or empirical approach is that the ratio of sulfate mass to the total mass of aerosols is constant, which is a gross simplification. Therefore in this paper we parameterize droplet nucleation as a function of total aerosol number concentration, updraft velocity and a parameter, which takes the aerosol distribution into account. The total number of aerosol particles is obtained as the sum of marine sulfate aerosols, hydrophylic organic and black carbon, submicron dust, and sea-salt aerosols. Anthropogenic sulfate only adds mass to the preexisting aerosols but does not form new particles.

As compared to the experiment with an empirical relationship between the number of cloud droplets and the mass of sulfate aerosols (DIAG), the shortwave cloud forcing simulated with the prognostic approach (PROG) is in better agreement with observations, the overestimation in the tropics is reduced, and the underestimation in the extratropics of the Southern Hemisphere is decreased. Because of fewer cloud droplets over the subtropical South and North Pacific in PROG than in DIAG the simulated liquid water path and shortwave cloud forcing with PROG reproduce the observed minima in that region. The simulated shortwave cloud forcing over the Southern Ocean in PROG agrees much better with ERBE than in DIAG, because the liquid water path is larger than in DIAG. It is, however, also larger than derived from SSM/I observations in this region. The effective radius, as derived from ISCCP,

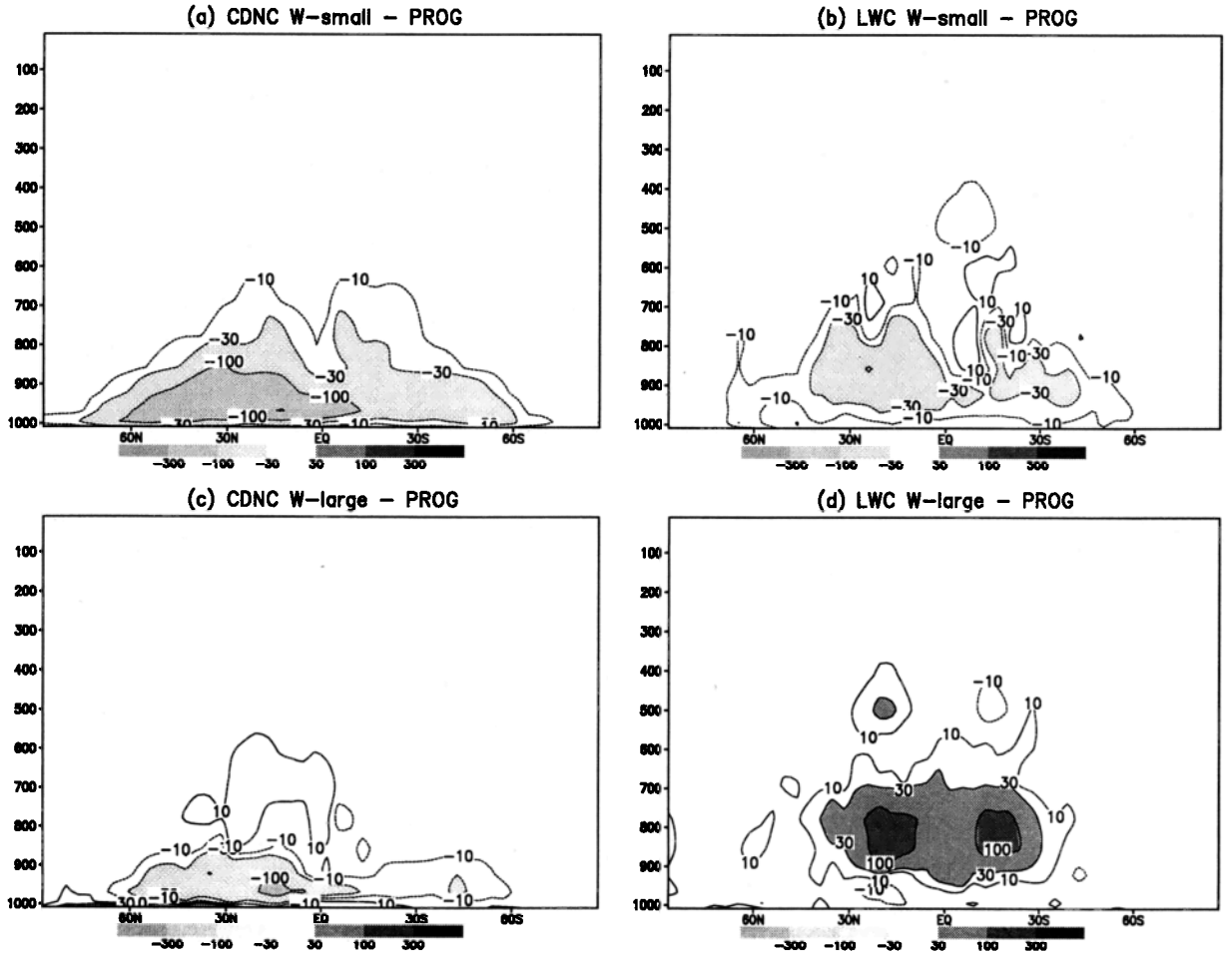


**Figure 13.** As Figure 11 but for the difference between sensitivity experiment W-small and PROG and between W-large and PROG.

suggests that the simulated effective radius is lower than observed in this region, but the column CDNC agrees well, which should result in a lower liquid water path than observed. This apparent contradiction might be either because the observations were taken during different years and the GCM was integrated with climatological sea surface temperature or because some of the simulated liquid water path originates from supercooled droplets in mixed-phase clouds, whereas column CDNC and effective radius are obtained from warm clouds only.

PROG captured the observed increase of cloud optical depth with increasing effective radius for optically thinner clouds ($\tau < 15$) and decrease of cloud optical depth with increasing effective radius for optically thicker marine clouds ($\tau > 15$). This is very encouraging insofar as for climate change studies it is at least as important to correctly simulate departures from the mean as the average value itself.

The sensitivity experiments showed that the number of cloud droplets in the boundary layer is very sensitive to the vertical velocity, the factor $\alpha$, and the spatial distribution of the total number of aerosol particles. The number of cloud droplets in 920 hPa is a factor of 3 smaller if the vertical velocity is 10 cm $s^{-1}$ everywhere, and twice as large if a constant value of $\alpha$ rather than the one obtained from the microphysical model is used. However, as the water vapor supply for cloud formation is dynamically controlled, most of the differences seen in the number of cloud droplets in individual levels do not change the liquid water path by more than 12%. Moreover, as most of the changes occur in the boundary layer, where the clouds are already optically thick and often obscured by overlying clouds, further increases in the number of cloud droplets as in the experiment $\alpha$-Ghan do not change the shortwave cloud forcing significantly.

Ideally, if the ratio of sulfate aerosol mass to the total aerosol mass is constant, the vertical profile of the number of cloud droplets obtained from PROG should match the one obtained from DIAG, as observations taken in many different weather regimes are used to derive the empirical relationship between the number of cloud droplets and the mass of sulfate aerosols (compare Figure 2). However, the vertical profile of CDNC

is much smoother in DIAG than in PROG and many more cloud droplets are present in DIAG above 900 hPa. Errors in DIAG can be due to an overestimation of the mass of sulfate aerosols in the free atmosphere or to the assumption of a constant fraction of the mass of sulfate to the total mass of aerosols, which is frequently violated. This will be investigated elsewhere as only recently observations of vertical profiles of sulfate aerosols have become available. As the number of aerosol particles in PROG in all layers is larger than suggested by *Jaenicke* [1993], the number of cloud droplets should be larger in PROG than in DIAG everywhere. As this is not the case, the sub-grid-scale vertical velocity, as derived from the turbulent kinetic energy, is probably too small above the boundary layer, activating very few cloud droplets or collision-coalescence or evaporation reduce the number of cloud droplets rapidly.

Given the uncertainty in obtaining the vertical velocity in a GCM, one could argue that at the present time an empirical approach is superior to the prognostic approach used here. However, several facts argue against a diagnostic approach.

1. With the prognostic approach we are able to treat the effect of in-cloud oxidation on aerosol number concentration more realistically. In a cloud, which neither precipitates nor evaporates, aqueous phase oxidation of $SO_2$ will neither change the number of aerosols nor change the number of cloud droplets. If aqueous phase oxidation of $SO_2$ takes place in DIAG, the mass of sulfate aerosols increases, and in the next time step, the cloud artificially has a higher number of cloud droplets. As this hinders precipitation formation, the lifetime of this cloud is artificially prolonged.

2. In DIAG the sulfate aerosol mass is a surrogate for the total mass of aerosols assuming a constant ratio of sulfate mass to the total mass of aerosols. To consider aerosol species other than sulfates in a diagnostic or empirical approach, empirical relationships are needed from measurement campaigns, where the number of cloud droplets is related to the full aerosol composition rather than just to sulfates. These measurements are not available yet.

3. Most importantly, empirical relationships are derived under present-day atmospheric conditions and might not be true in the case of a climatic change. Thus the physically based approach is superior to an empirical approach.

The assumption of a uniformly internally mixed aerosol clearly is a simplification. Theoretically, one must calculate the cloud droplet nucleation for many different aerosol particles, in which the composition of aerosols, the percentage of soluble matter, and the size vary. New data (F. Raes, personal communication, 1998) suggest that no saturation effect of the number of nucleated droplets is found for continental clouds, which would contradict the results from the microphysical model used for droplet nucleation in this study. To account for this effect and examine the cloud droplet nucleation with respect to aerosol composition and size is beyond the scope of this paper. Thus we have limited this paper to a study of the cloud droplet number in a GCM obtained from uniformly internally mixed aerosols. We show that the liquid water path and shortwave cloud forcing can be simulated realistically, if activation of all aerosols types is considered.

Another simplification clearly is to have prescribed dust and sea-salt aerosols, while carbonaceous aerosols and sulfate aerosols are treated prognostically. Thus the next step will be to introduce an aerosol microphysics scheme into the ECHAM GCM, and to treat all aerosol species in the same way. Then we will calculate different size categories for the different aerosol species and will be able to link droplet nucleation to accumulation and coarse mode size particles only. Larger-size sea-salt aerosols, for example, nucleate earlier than sulfate aerosols. Moreover, it is assumed that all soluble aerosols are subject to nucleation scavenging, whereas in reality, some smaller particles remain interstitial. This assumption is justified in terms of aerosol mass [*Flossmann,* 1996] but will have to be addressed when we consider aerosol number concentrations. These processes will be addressed in the future in order to handle interactions between different aerosol species with clouds more appropriately.

**Acknowledgments.** We thank Glen Lesins and Richard Leaitch for fruitful discussions and Qingyuan Han for providing the ISCCP data. We also thank Steve Ghan and one anonymous reviewer for helpful comments and suggestions. Ulrike Lohmann thanks the National Science and Engineering Research Council of Canada (NSERC) for support, Joyce Penner and Catherine Chuang thank the NASA Atmospheric Chemistry, Modeling, and Analysis Program, and Johann Feichter thanks the EC project ENV4-CT95-0099 (SINDICATE). Ulrike Lohmann and Joyce Penner also thank the Max-Planck-Institut für Meteorologie for extended visits. We thank the Deutsches Klimarechenzentrum (DKRZ) for computing time.

## References

Andreae, M. O., Climatic effects of changing atmospheric aerosol levels, in *Future Climates of the World: A Modelling Perspective*, vol. 16, World Survey of Climatology, edited by A. Henderson-Sellers, Elsevier, New York, 1995.

Beheng, K. D., A parameterization of warm cloud microphysical conversion processes, *Atmos. Res.*, *33*, 193–206, 1994.

Benkovitz, C. M., C. M. Berkowitz, R. C. Easter, S. Nemesure, R. Wagener, and S. Schwartz, Sulfate over the North Atlantic and adjacent continental regions: Evaluation for October and November 1986 using a three-dimensional model driven by observation-derived meteorology, *J. Geophys. Res.*, *99*, 20,725–20,756, 1994.

Boucher, O., and U. Lohmann, The sulfate-CCN-cloud albedo effect, a sensitivity study with two general circulation models., *Tellus, Ser. B*, *47*, 281–300, 1995.

Brinkop, S., and E. Roeckner, Sensitivity of a general circulation model to parameterizations of cloud-turbulence interactions in the atmospheric boundary layer, *Tellus, Ser. A*, *47*, 197–220, 1995.

Cachier, H., C. Liousse, M.-H. Pertuisot, A. Gaudichet,

F. Echalar, and J.-P. Lacaux, African fire particulate emissions and atmospheric influence, in *Biomass Burning and Global Change*, edited by J. S. Levine, pp. 428–440, MIT Press, Cambridge, Mass., 1996.

Chin, M., D. J. Jacob, G. M. Gardner, M. S. Foreman-Fowler, and P. A. Spiro, A global three-dimensional model of tropospheric sulfate, *J. Geophys. Res.*, *101*, 3761–3778, 1996.

Chuang, C. C., and J. E. Penner, Effects of anthropogenic sulfate on cloud drop nucleation and optical properties, *Tellus, Ser. B*, *47*, 566–577, 1995.

Chuang, C. C., J. E. Penner, K. E. Taylor, A. S. Grossmann, and J. J. Walton, An assessment of the radiative effects of anthropogenic sulfate, *J. Geophys. Res.*, *102*, 3761–3778, 1997.

Cooke, W. F., and J. J. N. Wilson, A global black carbon aerosol model, *J. Geophys. Res.*, *101*, 19,395–19,409, 1996.

Dentener, F., and P. J. Crutzen, A three-dimensional model of the global ammonia cycle, *J. Atmos. Chem.*, *19*, 331–369, 1994.

Eppel, D. P., H. Kapitzka, K. Claussen, D. Jacob, W. Koch, L. Levkov, H. T. Mengelkamp, and N. Werrmann, The non-hydrostatic mesoscale model GESIMA, 2, Parameterizations and applications., *Beitr. Phys. Atmos.*, *68*, 15–41, 1995.

Feichter, J., E. Kjellström, H. Rodhe, F. Dentener, J. Lelieveld, and G.-J. Roelofs, Simulation of the tropospheric sulfur cycle in a global climate model, *Atmos. Environ.*, *30*, 1693–1707, 1996.

Feichter, J., U. Lohmann, and I. Schult, The atmospheric sulfur cycle and its impact on the shortwave radiation, *Clim. Dyn.*, *13*, 235–246, 1997.

Flossmann, A., Mesoscale modelling of clouds and aerosol particles, in *XII NATO Challenges of Modern Society 21*, edited by S. E. Gryning and F. Schiermeier, pp. 259–273, Plenum, New York, 1996.

Fouquart, Y., and B. Bonnel, Computations of solar heating of the earth's atmosphere: A new parameterization, *Beitr. Phys. Atmos. 53*, 35-62, 1980.

Ganzeveld, L., J. Lelieveld, and G.-J. Roelofs, A dry deposition parameterization for sulfur oxides in a chemistry and general circulation model, *J. Geophys. Res.*, *103*, 5679–5694, 1998.

Ghan, S. J., C. C. Chuang, and J. E. Penner, A parameterization of cloud droplet nucleation, 1, Single aerosol type, *Atmos. Res.*, *30*, 197–221, 1993.

Ghan, S. J., L. R. Leung, R. C. Easter, and H. Abdul-Razzak, Prediction of cloud droplet number in a general circulation model, *J. Geophys. Res.*, *102*, 21,777–21,794, 1997.

Gillette, D. A., Are changes in dust sedimentation to polar regions a sign of dust production due to a climatic sensitive variable or more efficient atmospheric transport? And where does the dust come from? in *Precipitation, Scavenging and Atmospheric-Surface Exchange*, edited by S. E. Schwartz and W. G. N. Slinn, pp. 1719–1732, Hemisphere, Wash., 1992.

Gillette, D. A., and R. Passi, Modeling dust emission caused by wind erosion, *J. Geophys. Res.*, *93D*, 12,645–12,662, 1988.

Goudie, A. S., and G. L. Wells, The nature, distribution, and formation of pans in arid zones, *Earth Sci. Rev.*, *38*, 1–69, 1995.

Graf, H., J. Feichter, and B. Langmann, Volcanic sulfur emissions: Estimates of source strength and its contribution to the global sulfate distribution, *J. Geophys. Res.*, *102*, 10,727–10,738, 1997.

Greenwald, T. J., G. L. Stephens, T. H. Vonder Haar, and D. L. Jackson, A physical retrieval of cloud liquid water over the global oceans using special sensor microwave/imager (SSM/I) observations, *J. Geophys. Res.*, *98*, 18,471–18,488, 1993.

Guenther, A., et al., A global model of natural volatile organic compound emissions, *J. Geophys. Res.*, *100*, 8873–8892, 1995.

Gultepe, I., and G. A. Isaac, The relationship between cloud droplet and aerosol number concentrations for climate models, *Int. J. Climatol.*, *16*, 1–6, 1996.

Hallberg, A., K. J. Noone, and J. A. Ogren, Aerosol particles and clouds: which particles form cloud droplets, *Tellus, Ser. B*, *50*, 59–75, 1998.

Han, Q., W. B. Rossow, and A. A. Lacis, Near-global survey of effective droplet radii in liquid water clouds using ISCCP data, *J. Clim.*, *7*, 465–497, 1994.

Han, Q., W. B. Rossow, J. Chou, and R. Welch, Global survey of the relationship of cloud albedo and liquid water path with droplet size using ISCCP, *J. Clim.*, *11*, 1516–1528, 1998a.

Han, Q., W. B. Rossow, J. Chou, and R. Welch, Global variation of column droplet concentration in low-level clouds, *Geophys. Res. Lett.*, *25*, 1419–1422, 1998b.

Hao, W. M., M. H. Liu, and P. J. Crutzen, Estimates of annual and regional releases of $CO_2$ and other trace gases to the atmosphere from fires in the tropics, based on the FAO statistics for the period 1975-80, in *Fire in the tropical biota. Ecosystem processes and global challenges*, edited by J. G. Goldammer, pp. 440–462, Springer-Verlag, New York, 1990.

Hegg, D. A., R. J. Ferek, and P. V. Hobbs, Light scattering and cloud condensation nucleus activity of sulate aerosol measured over the northeast Atlantic Ocean, *J. Geophys. Res*, *98*, 18,727–18,733, 1993.

Hegg, D. A., R. J. Ferek, P. V. Hobbs, and A. P. Waggoner, Measurements of some aerosol properties relevant to radiative forcing on the east coast of the United States, *J. Appl. Meteorol.*, *34*, 2306–2315, 1995.

Houghton, J. T., L. G. M. Filho, B. A. Callander, N. Harris, A. Kattenberg, and K. Maskell (Eds.), Climate change 1995, in *The science of climate change, Intergovernmental Panel on Climate*, Cambridge Univ. Press, New York, 1996.

Hudson, J. G., and C. F. Rogers, Relationship between critial supersaturation and cloud droplet size: Implications for cloud mixing processes, *J. Atmos. Sci.*, *43*, 2341–2359, 1986.

Husar, R., J. M. Prospero, and L. L. Stowe, Characterization of tropospheric aerosols over the oceans with the NOAA advanced very high resolution radiometer optical thickness operational product, *J. Geophys. Res.*, *102*, 16,889–16,909, 1997.

Jaenicke, R., Aerosol physics and chemistry, in *Landolt-Bornstein, New Ser.*, vol. V/4b, pp. 391–457, Springer-Verlag, New York, 1988.

Jaenicke, R., Tropospheric aerosols, in *Aerosol-Cloud-Climate Interactions Int. Geophys. Ser.*, vol. 54, edited by P. V. Hobbs, pp. 1–31, Academic, San Diego, Calif., 1993.

Johnson, D. W., Parameterisation of the cloud-topped boundary layer: Aircraft measurements, in *Proceedings of a workshop on Parameterisation of the Cloud-Topped Boundary Layer*, Eur. Cent. for Medium-Range Weather Forecasts, Reading, England, 1993.

Jones, A., D. L. Roberts. and A. Slingo, A climate model study of indirect radiative forcing by anthropogenic sulphate aerosols, *Nature*, *370*, 450–453, 1994.

Joussame, S., Three-dimensional simulations of the atmospheric cycle of desert dust particles using a general circulation model, *J. Geophys. Res.*, *95*, 1909–1941, 1990.

Kessler, E., On the distribution and continuity of water substance in atmospheric circulations, *Meteorol. Monogr.*, vol. 10, 84 pp., Am. Meteorol. Soc., Boston, Mass., 1969.

Kettle, A. J., et al., A preliminary global database of sea surface dimethyl sulfide measurements and a simple model to predict sea surface dimethyl sulfide as a function of latitude, longitude, and month, *EOS Trans. AGU, 77 (46)*, 417, Fall Meet. Suppl., 1996.

Köpke, P., M. Hess, I. Schult, and E. P. Shettle, Global aerosol data set, *Tech. Rep. 243*, Max-Planck-Inst. für Meteorol., Hamburg, Germany, 1997.

Kogan, Z. N., and D. K. Kogan, and Y. L. Lilly, Cloud factor and seasonality of the indirect effect of anthropogenic sulfate aerosols, *J. Geophys. Res., 102*, 25,927–25,939, 1997.

Levkov, L., B. Rockel, H. Kapitza, and E. Raschke, 3D mesoscale numerical studies of cirrus and stratus clouds by their time and space evolution, *Beitr. Phys. Atmos., 65*, 35–58, 1992.

Li, S.-M., C. M. Banic, W. R. Leaitch, P. S. K. Liu, G. A. Isaac, X.-L. Zhou, and Y.-N. Lee, Water-soluble fractions of aerosol and their relations to number size distributions based on aircraft measurements from the north atlantic regional experiment., *J. Geophys. Res., 101*, 29,111–29,121, 1996.

Lin, H., and W. R. Leaitch, Development of an in-cloud aerosol activation parameterization for climate modelling, in *Proceedings of the WMO Workshop on Measurement of Cloud Properties for Forecasts of Weather, Air Quality and Climate*, World Meteorol. Organ., Geneva, 1997.

Lin, Y. L., R. D. Farley, and H. D. Orville, Bulk parameterization of the snow field in a cloud model, *J. Clim. Appl. Meteorol., 22*, 1065–1092, 1983.

Liousse, C., J. E. Penner, C. Chuang, J. J. Walton, H. Eddleman, and H. Cachier, A global three-dimensional model study of carbonaceous aerosols, *J. Geophys. Res., 101*, 19,411–19,432, 1996.

Liss, P. S., and L. Merlivat, Air-sea gas exchange rates: Introduction and synthesis, in *The Role of Air-Sea Exchange in Geochemical Cycling*, D. Reidel, Norwell, Mass., 1996.

Lohmann, U., and J. Feichter, Impact of sulfate aerosols on albedo and lifetime of clouds: A sensitivity study with the echam gcm, *J. Geophys. Res., 102*, 13,685–13,700, 1997.

Lohmann, U., and E. Roeckner, Design and performance of a new cloud microphysics scheme developed for the ECHAM general circulation model, *Clim. Dyn., 12*, 557–572, 1996.

Lohmann, U., N. McFarlane, L. Levkov, K. Abdella, and F. Albers, Comparing different cloud schemes of a single column model by using mesoscale forcing and nudging technique., *J. Clim., 12*, 438–461, 1999.

Malm, W. C., J. F. Sisler, D. Huffmann, R. A. Eldred, and T. A. Cahill, Spatial and seasonal trends in particle concentration and optical extinction in the United States., *J. Geophys. Res., 99*, 1347–1370, 1994.

Monahan, E. C., D. E. Spiel, and K. L. Davidson, A model of marine aerosol generation via whitecaps and wave disruption, in *Oceanic Whitecaps*, edited by E. C. Monahan and G. Mac Niocaill, D. Reidel, Norwell, Mass., 1986.

Morcrette, J. J., Radiation and cloud radiative properties in the European Centre for Medium Range Weather Forecasts forecasting system, *J. Geophys. Res., 96*, 9121–9132, 1991.

Nickling, W. G., and J. A. Gilles, Emission of fine-grained particluates from desert soils, in *Paleoclimatology and Paleometeorology: Modern and Past Petterns of Global Atmospheric Transport*, edited by M. Leinen and M. Sarnthein, pp. 133–165, Kluwers, Acad., Norwell, Mass., 1989.

Nordeng, T. E., Extended versions of the convective parameterization scheme at ECMWF and their impact on the mean and transient activity of the model in the tropics, *Tech. Memo. 206*, Eur. Cent. for Medium-Range Weather Forecasts, Reading, England, 1994.

Ogura, Y., and T. Takahashi, Numerical simulation of the life cycle of a thunderstorm cell, *Mon. Weather Rev., 99*, 895–911, 1971.

Pavia, E. G., and J. J. O'Brien, Weibull statistics of wind speed over the ocean, *J. Clim. Appl. Meteorol., 25*, 1324–1332, 1986.

Penner, J. E., H. Eddleman, and T. Novakov, Towards the development of a global inventory of black carbon emissions, *Atmos. Environ., 27*(A), 1277–1295, 1993.

Pham, M., J.-F. Mueller, G. P. Brasseur, C. Granier, and G. Megie, A three-dimensional study of the tropospheric sulfur cycle, *J. Geophys. Res., 100*, 26,061–26,092, 1995.

Phillips, T. J., A summary documentation of the AMIP models, program for climate model diagnosis and intercomparison, *Tech. Rep. 18*, Univ. of Calif., Lawrence Livermore Nat. Lab., Livermore, 1994.

Prospero, J. M., Mineral and sea-salt aerosol concentrations in various ocean regions, *J. Geophys. Res., 84*, 725–731, 1979.

Prospero, J. M., M. Uematsu, and D. L. Savoie, Mineral aerosol transport to the Pacific Ocean, in *Chemical Oceanography*, edited by J. P. Riley, and R. Chester, pp. 188–218, Academic, San Diego, Calif., 1989.

Pruppacher, H. R., and J. D. Klett, *Microphysics of Clouds and Precipitation*, D. Reidel, Hingham, Massachusetts, 1978.

Pye, K., *Aeolian Dust and Dust Deposits*, Academic, London, 1987.

Rasch, P. J., and D. L. Williamson, Computational aspects of moisture tranport in global models of the atmosphere, *Q. J. R. Meteorol. Soc., 116*, 1071–1090, 1990.

Rea, D. K., The paleoclimatic record provided by eolian deposition in the deep sea: The geologic history of wind, *Rev. Geophys., 32*, 159–195, 1994.

Rockel, B., E. Raschke, and B. Weyres, A parameterization of broadband radiative transfer properties of water, ice and mixed clouds, *Beitr. Phys. Atmos., 64*, 1–12, 1991.

Roeckner, E., et al., The atmospheric general circulation model ECHAM4: Model description and simulation of the present-day climate, *Tech. Rep. 218*, Max-Planck-Inst. für Meteorol., Hamburg, Germany, 1996.

Roelofs, G.-J., and J. Lelieveld, Distribution and budget of $O_3$ in the troposphere calculated with a-chemistry general circulation model, *J. Geophys. Res., 100*, 20,983–20,998, 1995.

Roelofs, G.-J., J. Lelieveld, and R. v. Dorland, Simulation of global sulfate distribution and the influence on effective cloud drop radii with a coupled photochemistry-sulfur cycle model, *Tellus, Ser. B., 50*, 224–242, 1998.

Rossow, W. B., and R. A. Schiffer, ISCCP cloud data products, *Bull. Am. Meteorol. Soc., 72*, 2–20, 1991.

Rotstayn, L. D., Indirect forcing by anthropogenic aerosols: A global climate model calculation of the effective-radius and cloud-lifetime effects, *J. Geophys. Res.*, in press, 1999.

Schütz, L., Saharan dust transport over the North Atlantic Ocean–Model calculations and measurements, in *Saharan Dust*, edited by C. Morales, pp. 267–277, John Wiley, New York, 1979.

Sehmel, G. A., Deposition and resuspension, in *Atmospheric Science and Power Production*, edited by D. Randerson, *Rep. DOE/TIC-27601 (DE84005177)*, pp. 533–583, Nat. Tech. Inf. Cent., Springfield, Va., 1984.

Slinn, S. A., and W. G. N. Slinn, Predictions for particle deposition on natural waters, *Atmos. Environ., 14*, 1013–1016, 1980.

Smith, D. M., M. S. Akhter, J. A. Jassim, C. A. Sergides,

W. F. Welch, and A. R. Chughtai, Studies of the structure and reactivity of soot, *Aerosol Sci. Technol.*, *10*, 311–325, 1989.

Spiro, P. A., D. J. Jacob, and J. A. Logan, Global inventory of sulfur emissions with 1° x 1° resolution, *J. Geophys. Res.*, *97*, 6023, 1992.

Tang, I. N., Chemical and size effects of hygroscopic aerosols on light scattering coefficients, *J. Geophys. Res.*, *101*, 19,245–19,250, 1996.

Tegen, I., and I. Fung, Modeling of mineral dust in the atmopshere: Sources, transport, and optical thickness, *J. Geophys. Res.*, *99*, 22,897–22,914, 1994.

Tegen, I., P. Hollrig, M. Chin, I. Fung, D. Jacob, and J. Penner, Contribution of different aerosol species to the global aerosol extinction optical thickness: Estimates from model results, *J. Geophys. Res.*, *102*, 23,895–23,915, 1997.

Tiedtke, M., A comprehensive mass flux scheme for cumulus parameterization in large-scale models, *Mon. Weather Rev.*, *117*, 3040–3061, 1989.

Warneck, P., *Chemistry of the Natural Atmosphere*, vol. 41, *Int. Geophys. Ser.*, Academic, San Diego, Calif., 1998.

Webb, R. S., C. E. Rosenweig, and E. R. Levine, Specifying land surface characteristics in general circulation models: Soil profile data set and derived water-holding capacities, *Global Biogeochem. Cycles*, *7*, 97–108, 1993.

Weng, F., and N. C. Grody, Retrieval of cloud liquid water using the special sensor microwave imager (SSM/I), *J. Geophys. Res.*, *99*, 25,535–25,551, 1994.

Westphal, D. L., O. B. Toon, and T. N. Carlson, A case study of mobilization and transport of saharan dust, *J. Atmos. Sci.*, *45*, 2145–2175, 1988.

Wyser, K., The effective radius in large-scale models: Impact of aerosols and coalescence, *Atmos. Res.*, *49*, 213–234, 1998.

Yum, S. S., J. G. Hudson, and Y. Xie, Comparisons of cloud microphysics with cloud condensation nuclei spectra over the summertime Southern Ocean, *J. Geophys. Res.*, *103*, 16,625–16,636, 1998.

---

U. Lohmann, Atmospheric Science Program, Department of Physics, Dalhousie University, Halifax, N. S., B3H 3J5, Canada. (Ulrike.Lohmann@Dal.Ca)

J. Feichter, Max Planck Institute for Meteorology, Bundesstr.55, D-20146 Hamburg, Germany

C. Chuang, Lawrence Livermore National Laboratory, 7000 East Ave., Livermore, CA 94550.

J. Penner, Departments of Atmospheric, Oceanic, and Space Sciences, University of Michigan, 2455 Hayward, Ann Arbor, MI 48109-2143.

(Received August 16, 1998; revised November 30, 1998; accepted January 21, 1999.)